# Recruitment of TRiC chaperonin in rotavirus viroplasms directly associates with virus replication.

Janine Vetter[a], Guido Papa[b,*], Kurt Tobler[a], Manuel Kley[a], Michael Myers[c], Mahesa Wiesendanger[a,d], Elisabeth M. Schraner[a,d], Oscar R. Burrone[b], Cornel Fraefel[a], Catherine Eichwald[a,#]

[a] Institute of Virology, University of Zurich, Zurich, Switzerland

[b] Molecular Immunology Lab, International Centre for Genetic Engineering and Biotechnology, Trieste, Italy

[c] Proteomics Lab, International Centre for Genetic Engineering and Biotechnology, Trieste, Italy

[d] Institute of Veterinary Anatomy, University of Zurich, Zurich, Switzerland

Running Head: TRiC regulates rotavirus replication

#Address correspondence to Catherine Eichwald, ceichwald@vetvir.uzh.ch

*Present address: MRC Laboratory of Molecular Biology, Cambridge, United Kingdom.

## Abstract

Rotavirus replication takes place in the viroplasms, which are cytosolic inclusions allowing the synthesis of virus genome segments, followed by their encapsidation in the core shell and the addition of the second layer of the virion. The viroplasms are composed of several viral proteins, including NSP5, which is the main building block. Microtubules, lipid droplets, and miRNA-7 are among the host components recruited in viroplasms. Aiming to investigate the relationship between rotavirus proteins and host components in the viroplasms, we performed a pull-down assay of lysates from rotavirus-infected cells expressing NSP5-BiolD2. Subsequent tandem mass spectrometry identified all eight subunits of the TRiC complex, a cellular chaperonin responsible for folding at least 10% of the cytosolic proteins. Our validated results show that TriC is recruited in viroplasms and there specifically surrounds newly formed double-layered particles (DLPs). Chemical inhibition of TRiC and silencing of its subunits drastically reduced virus progeny production.

Interestingly, TRiC-inhibited RV-infected cells lacked TLPs but harbored empty DLPs. Using sequence-specific direct RNA nanopore sequencing, we demonstrate that TRiC is essential for RV replication since it modulates dsRNA genome segment synthesis, specifically (-)RNA. Moreover, TRiC is associated with RNA-dependent RNA polymerase, VP1, and regulates the folding of VP2, a cofactor allowing dsRNA synthesis. This study provides *in vivo* evidence of the regulatory mechanism by which dsRNA genome segment replication is controlled and coordinated in the rotavirus viroplasms.

## Importance.

The replication of rotavirus takes place in cytosolic inclusions termed viroplasms. In these inclusions, the eleven double-stranded RNA genome segments are synthesized and packaged individually into the newly generated virus particles. In this study, we show for the

48 first time that the TRiC complex, a cellular chaperonin responsible for the folding of at least
49 10% of the cytosolic proteins, is a component of viroplasms and is required for the synthesis
50 of the viral (-)ssRNA. Specifically, TRiC interacts with VP1, the RNA-dependent RNA
51 polymerase, and assists in the folding of VP2, the cofactor involved in RNA replication. Our
52 study adds a new component to the current model of rotavirus replication, where TRiC is
53 recruited in viroplasm to assist replication.
54

## Introduction

Virus factories are compartmentalized inclusions made during the virus life cycle to assemble the replication factors to generate virus progeny. For example, rotavirus (RV), a multisegmented double-stranded RNA (dsRNA) virus and member of the Reoviridae family, replicates in the so-called viroplasms. These structures are composed of several RV proteins and ss- and dsRNAs appearing as cytosolic membrane-less electron-dense inclusions when visualized at the electron microscope (1-3). Several essential processes for the RV life cycle take place in the viroplasms corresponding to the replication and packaging of the eleven dsRNA genome segments (gs) in newly formed VP2 icosahedral core-shells. This process is assisted by replication intermediates composed of the RNA-dependent RNA polymerase (RdRp), VP1, and the helicase and guanylyl-methyltransferase VP3, which are found underneath each of the core-shell five-fold axis (4, 5). VP2 also acts as a cofactor of VP1, at least *in vitro*, for the dsRNA synthesis (6). The nonstructural proteins NSP5 and NSP2 take part in this replication step because they associate with VP1 in a mechanism that is still not completely elucidated (7-9). Subsequently, the filled core shells are coated by a second protein layer of VP6 trimers forming double-layered particles (DLP), which bud to the adjacent endoplasmic reticulum (ER) to acquire its outer coat. The triple-layered particles (TLP) are composed of glycoprotein VP7 and spike protein VP4, which can be found with transient lipid membranes in the ER surrounding the viroplasms (10). Moreover, the viroplasms, when detected by fluorescence microscopy, appear as cytosolic globular inclusions that are homogeneously distributed in the cell at early times post-infection (~4 hpi). The main building block for viroplasm formation is NSP5 (11-13), specifically, its hyperphosphorylated isoform was shown to be essential for forming viroplasms (7, 14-16). Additionally, phosphorylated NSP2 is a requirement for viroplasm formation as well (9, 17). Interestingly, the co-expression of NSP5 with either NSP2 or VP2 is sufficient to build

viroplasm-like structures (VLS) (12, 18, 19) which are morphologically identical to viroplasms, but lack virus replication components and hence are unable to produce virus progeny. The VLSs are excellent simplified tools for studying the complex viroplasm organization.

It has been demonstrated that viroplasms are highly dynamic, being able to coalesce between them and move to the juxtanuclear region of the cell at increasing times post-infection (20-22). Furthermore, despite not yet being well-defined, several host factors have been identified as necessary for viroplasm formation and maintenance (21, 23-26). On one side, the initiation process for viroplasm formation requires a scaffold of lipid droplets by incorporating perilipin-1 (27, 28). Furthermore, the host cytoskeleton, actin filaments and microtubules, plays a role in the formation, maintenance, and dynamics of the viroplasms (21, 29, 30). In this context, NSP2 octamers directly associate with microtubules to promote viroplasm coalescence (8, 21, 31-33). Moreover, VP2 plays a role in viroplasm dynamics by allowing their perinuclear motion (21). Finally, consistent with the above-described features, the viroplasms have been recently attributed as liquid-liquid phase-separated structures (34).

The RdRp (VP1) shares a unique feature with all described RdRp enzymes of the Reoviridae family (35-38) that it consists of four channels that connect the catalytic cavity with the exterior corresponding to template entry, NTP entry, transcript exit, and template exit (39). This enzyme transcribes from DLPs the mRNA or positive-sense single-stranded RNA ((+)ssRNA) using as a template the negative-sense single stranded RNA ((-)ssRNA) obtained by unwinding the dsRNA genome segments via the C-terminal domains (40, 41). Also, *in vitro* experiments have shown that purified VP1 synthesizes dsRNA using (+)ssRNA as a template by recognizing the 3' consensus sequence of each genome segment in a process strictly assisted by purified VP2 (6, 42). Thus, there is no *in vivo* evidence yet identifying this essential mechanism for the encapsidation of the newly generated genome segments.

105 The eukaryotic group II chaperonin tailless complex polypeptide I ring complex
106 (TRiC) engages in the folding of at least 10% of all cytosolic proteins. It mainly favors the
107 folding of newly translated proteins with complex beta-sheet topologies, such as actin and
108 tubulin, and cell cycle regulators (43). Although, TRiC has a continuously increasing list of
109 client proteins that are involved in diverse cellular processes (44, 45). TRiC is organized as
110 two back-to-back hetero-octameric rings having a barrel-shaped structure enclosing an ATP-
111 dependent folding chamber. Each of these rings comprises eight paralog subunits (CCT1-
112 CCT8) that tweak according to the specificity required for client proteins through differential
113 recognition modes and differentiate rates of ATP binding and hydrolysis between the ring
114 subunits (44, 46). Recently, TRiC activity also has been found to assist the folding of several
115 viral proteins involved in various steps of the virus life cycle, such as entry (47), virus
116 replication (48-54), virion assembly (55, 56) and virus particle release (57).

117 In this study, we demonstrate that TRiC is essential for RV replication by being
118 recruited to viroplasms, where it modulates dsRNA genome segment synthesis, specifically (-
119 )ssRNA. Furthermore, we reveal that TRiC is associated with RdRp (VP1) and regulates the
120 folding of VP2, a cofactor for dsRNA synthesis. Finally, we provided *in vivo* evidence of the
121 regulatory mechanism of RV dsRNA synthesis mediated by RdRp.

122

## 123 Results

124 **Association of TRIC components to NSP5-BioID2**. To assess the interaction of rotavirus
125 proteins and host components in the viroplasms, we generated a stable MA104 cell line,
126 MA/NSP5-BioID2, expressing NSP5 fused to BioID2, a promiscuous biotin ligase for the
127 detection of protein-protein associations and proximate proteins in living cells (58). As
128 expected (7, 20, 21), NSP5-BioID2 localizes and accumulates upon RV-infection into
129 viroplasms as visualized by the colocalization of streptavidin (StAV)-dylight 488 with VP2, a

130 marker for viroplasms at 6 and 24 hpi **(Fig 1A)**. Next (**Fig 1B**), we analyzed cell extracts of
131 RV-infected MA/NSP5-BioID2 cells at either 5 or 21 hpi by immunoblotting. We found that
132 most biotinylated proteins accumulate in cell extracts prepared at 21 hpi rather than at 5 hpi.
133 Moreover, the bands consistent with the predicted molecular weight of NSP5, NSP2, and
134 VP2 appeared at this specific time upon RV infection. The 21 hpi cell extracts were pulled
135 down with StAv conjugated to magnetic beads and analyzed by label-free tandem mass
136 spectrometry (MS/MS) (**Fig 1C and Table 1**) that enabled the identification of 272 proteins.
137 The distribution of non-infected and RV-infected samples is illustrated in the rank order plot
138 of **Fig 1C**. Consistent with previous publications (14, 20, 29, 59, 60) and validating our
139 experimental procedure, NSP5-BioID2 pulled down RV proteins NSP5, NSP2, VP2, and
140 VP1, which are recognized protein-protein interactors with NSP5. Interestingly, our study
141 also identified the eight subunits (CCT1 to CCT8) of the T-complex protein-1 ring complex
142 (TRiC), a eukaryotic cytosolic ATP-dependent chaperonin that assists the folding of up to
143 10% of cytosolic proteins (45, 61).

144 **TRiC localizes in viroplasms and surrounding DLPs.** To validate our mass spectrometry
145 analysis, we investigated whether TRiC localizes into viroplasms at 6 hpi. As visualized with
146 immunofluorescence confocal microscopy (**Fig 2a)**, TRiC subunits CCT1, CCT2, and CCT3
147 colocalize with NSP5, a viroplasm marker, suggesting that TRiC is recruited to viroplasms.
148 Next, we also analyzed viroplasms at high-resolution using immune electron microscopy by
149 co-immunostaining of anti-CCT3 (12 nm gold particles) with either anti-NSP5 (6 nm gold
150 particles, **Fig 2b**) or anti-VP6 (6 nm gold particles, **Fig 2c**). Interestingly, CCT3, in addition
151 to localizing in viroplasms, was found in some cases rimming structures resembling DLPs by
152 their morphology and size and because VP6 surrounds them. Interestingly, NSP5 and CCT3
153 are also found rimming these globular structures.

154 **Inhibition of TRiC hampers viroplasm formation and RV replication.** We used a recently
155 described chemical TRiC inhibitor (62) (PubChem CID: 658022) corresponding to 2-[(4-
156 chloro-2λ4,1,3-benzothiadiazol-5-yl)oxy]acetic acid, shortly named TRICi, to investigate the
157 role of TRiC chaperonin in the RV life cycle. TRICi was validated in MA104 cells for its
158 ability to halt the onset of mitosis by impairing Cdc20 expression **(Fig S1a-e),** a well-
159 described protein dependent on TRiC for folding (63). When inspecting viroplasms at 6 hpi, a
160 time-frame for visualization of well-formed viroplasms (21), RV-infected cells treated at
161 early time post-infection (1 hpi) with TRICi showed significantly reduced numbers and size
162 of viroplasms per cell (**Fig 3a, b, and c**). In contrast, the addition of TRICi at 5 hpi showed
163 no changes in the morphology and number of viroplasms compared to untreated samples (**Fig**
164 **3a**). The TRICi treatment was not cytotoxic at the concentrations used in our experiments
165 **(Fig S1f)**. Notably, the impairment in viroplasm formation after TRiC inhibition was
166 observed for at least three RV strains, including porcine strain OSU and simian strains SA11
167 and RRV (**Fig S2**). The virus progeny was largely impaired (> 5 log) when TRICi was added
168 at 1 hpi at both tested concentrations but not when added at 5 hpi **(Fig 3d)**. Similarly, the
169 silencing of either CCT3 or CCT2 subunits significantly reduced virus progeny **(Fig S3a-d)**.
170 Consistent with the lack of virus progeny, we observed a complete depletion of the RV
171 dsRNA genome segments (**Fig 3e**) after TRICi treatment (lanes 2 and 3) when compared to
172 untreated cells (lane 1).

173 Additionally, the effect of TRICi on viroplasms was partially reversible when added
174 at 1 hpi and washed out at 2, 3, 4, or 5 hpi (**Fig S4a-e**), followed by analysis at 6 hpi. Large
175 viroplasms recovered even when removing the drug at 4 hpi, reaching the same levels as
176 untreated samples. Meanwhile, the number of small viroplasms did not recover even after
177 only 1 h of treatment with TRICi, remaining in large numbers distributed in the cytosol of the
178 infected cells. Besides, the expression of diverse RV proteins was recovered after removing

179 TRICi **(Fig S4f)**, which collectively suggests a delay in the coalescence of viroplasms
180 because of a lack of RV protein supplies required for building the inclusions. Additionally,
181 the distribution of diverse RV proteins was compared in untreated and TRICi-treated
182 conditions by immunofluorescence at 6 hpi. As observed in **Fig 3f**, RV viroplasm proteins
183 NSP5, NSP2, VP2, and VP6 delocalized from the virus factories and dispersed throughout
184 the cytosol, while VP1, NSP4, VP7, and VP4 did not show perceptible changes from their
185 characteristic distribution. Also, NSP3 showed dramatic changes with a dispersed
186 distribution.

187 **TRiC inhibition hampered RV packaging and TLP formation.** To investigate in detail the
188 decrease in both dsRNA genome segments and virus progeny associated with TRiC
189 inhibition, we examined the viroplasms by high-resolution electron microscopy at 6 hpi after
190 treatment with TRICi from 1 hpi. Surprisingly **(Fig 4a)**, we observed that viroplasms of both
191 untreated and TRICi-treated samples were electron dense. As expected, the endoplasmic
192 reticulum (ER) surrounding the viroplasms in the untreated sample was filled with TLPs at
193 diverse stages of maturation. Meanwhile, TRICi-treated samples showed almost empty ER
194 with a few immature virus particles. We then analyzed the virus particles isolated at 24 hpi
195 from cells treated with TRICi at 1 hpi or untreated to gain insights into virion structure and
196 composition. We found that the negatively stained virus particles from TRICi-treated cells
197 had an average size of 59 nm, consistent with the size and shape of DLPs. In contrast, the
198 virus particles from untreated cells had an average size of 72 nm, consistent with the size of
199 TLPs **(Fig 4b)**. Additionally, the virus particles isolated from TRICi-treated cells lacked the
200 outer layer proteins VP7 and VP4 **(Fig 4c**), contrasting with the virus particles from untreated
201 cells that contained all TLP components. More importantly, particles from TRICi-treated
202 cells also lacked VP1 and dsRNA genome segments and had a reduced association with
203 NSP2 (64)**(Fig 4 c and d)**.

204 **TRiC is required for (-)ssRNA synthesis.** We next hypothesized that TRiC inhibition
205 blocks the synthesis of (-)ssRNA but not (+)ssRNA. To assess this possibility, we established
206 a method for direct RNA sequencing for RV dsRNA to read both positive- and negative-
207 sense RNA strands using MinION Oxford nanopore technology (ONT) (65). For this
208 purpose, we designed specific reverse transcriptase adapters (RTA) that anneal to the 3' ends
209 of both positive and negative-sense RNA strands of the eleven genome segments of porcine
210 RV strain OSU **(Table S2)**. Total RNA from OSU-infected cells at 6 hpi was harvested and
211 sequenced via MinION to determine the effectiveness of the modified adapter. The sequence
212 runs covered 100% of the eleven genome segments of both positive- and negative-sense RNA
213 strands **(Fig 5a)**. The average coverage depth for the positive-sense RNA strands ranked from
214 7987.09 for gs 8 (NSP2) to 528.93 for gs5 (NSP1), while the negative-sense RNA strands
215 ranked from 1632.10 for gs 11 (NSP5) to 132.48 for gs 4 (VP4), respectively **(Table 2)**. The
216 average read level of accuracy of the eleven genome segments was 91.28 ± 0.46 % and
217 90.05± 0.58% for the positive- and negative-sense RNA strands, respectively. Meanwhile,
218 the consensus sequence coverage corresponded to 99.47±0.32% for the positive-sense RNA
219 strands and 99.28±0.41% for negative-sense RNA strands, in concordance with the consensus
220 sequence of the eleven genome segments provided for the RV strain OSU. The distribution of
221 positive-and negative-sense RNA strands read lengths **(Fig 5b)** correspond well to the
222 expected length of each respective segment. An odd cumulative ratio **(Fig 5c)** was
223 determined between the distribution of positive and negative sense RNA strand reads for each
224 genome segment with an accumulative value of 453. We then harvested RNA at 6 hpi from
225 RV-infected cells either untreated (DMSO) or treated with TRICi and followed direct RNA
226 sequencing of both positive- and negative-sense RNA strands. The sample from DMSO-
227 treated cells showed a complete coverage for both positive- and negative-sense RNA strands
228 (**Fig 5d, upper panel; Table 3**), with a similar distribution pattern observed for the above

229 mock sample (**Fig 5b, e, and f)**. However, the samples from TRICi-treated cells, although
230 showing similar depth coverage for all the eleven positive-sense strands as for DMSO
231 samples, denoted a highly reduced coverage for the eleven negative-sense strand RNAs **(Fig**
232 **5, lower panel)**. Even if the distribution of the eleven genome segments for positive-sense
233 RNA strand reads **(Fig 5e)** was comparable between samples from untreated and TRICi-
234 treated cells, it was highly diverse for the negative-sense reads **(Fig 5f)**. More precisely, the
235 numbers of negative-sense RNA strand reads were at least three times lower in the TRICi-
236 treated samples compared to the untreated samples. The ratio of positive-/negative-sense
237 RNA strand reads **(Fig 5g)** for DMSO-treated cells had a value of 509, similar to the above-
238 described value, while that of the TRICi-treated cells was much higher with a value of 1897,
239 suggesting a preponderance of (+)ssRNA reads among the TRICi sample.

240 **TRiC associates with VP1 and VP2.** As (-)ssRNA synthesis is impaired upon TRiC
241 inhibition, we wondered if other viroplasm components are associated with TRiC in addition
242 to NSP5. To assess this option, we took profit of an already well-described (66-69) *in vivo*
243 protein-protein interaction assay based on the ability of the C-terminal region of reovirus
244 protein μNS (amino acids 471-721) to form spontaneous cytosolic inclusions. In this
245 particular assay, we used as bait red monomeric mCherry fused to the N-terminus of (471-
246 721) μNS, herein mCh-μNS. The RV proteins (VP1, VP2, VP3, VP4, VP6, NSP2, and
247 NSP5) were fused at the N-terminus of mCh-μNS **(Fig S5a)**. Specific antibodies targeting
248 subunits for TRiC were used as fish. The colocalization visualized by the fluorescence
249 microscopy of the fish target protein with the RV protein-mCh-μNS cytosolic platform was
250 considered as a positive protein-protein interaction. In the first instance **(Fig 6a)**, we
251 examined the ability of the CCT3 subunit to colocalize with the mCh-μNS, which resulted as
252 expected negative. However, CCT3 was clearly associated with VP1-mCh-μNS, VP2-mCh-
253 μNS, and NSP5-mCh-μNS and only partially with NSP2-mCh-μNS and VP6-mCh-μNS. No

254 association was observed for CCT3 with VP3-mCh-μNS, VP4-mCh-μNS, and VP6-mCh-
255 μNS. Additionally, we confirmed the association of VP1-mCh-μNS and VP2-mCh-μNS with
256 TRiC subunit CCT1 **(Fig 6b)**. Interestingly, we found that TRiC subunit CCT2 **(Fig 6c)** is
257 associated with VP1-mCh-μNS but not with VP2-mCh-μNS. These results suggest that VP1
258 is the main RV protein associated with TRiC.

259 To further confirm the association of VP1 with TRiC, we formed viroplasm-like
260 structures (VLS) based on the co-expression of NSP5 with either NSP2 and VP2 (12, 18) and
261 monitored the recruitment of the TRiC subunit CCT3 by confocal immunofluorescence. We
262 found mild or no localization of CCT3 in either VLSs induced by NSP2 or VP2 **(Fig 7a)**.
263 Similarly, CCT3 was not recruited in VLSs induced by co-expression of either three (NSP5,
264 NSP2, and VP2) or four (NSP5, NSP2, VP2, and VP6) viroplasm proteins. However, VLSs
265 induced by co-expression of NSP5 with either NSP2 and VP1 or VP2 and VP1 significantly
266 increased the recruitment of CCT3 in the VLS inclusions. Next, we confirmed these results
267 **(Fig 7b)** by monitoring the recruitment of diverse TRiC subunits in VLSs formed by NSP5
268 and NSP2 co-expressed with or without a V5-tagged version of VP1 (V5-VP1). The results
269 showed that adding V5-VP1 into VLSs enhanced the recruitment of all the TRiC subunits
270 tested, including CCT1, CCT2, and CCT3. Similarly, the recruitment of TRiC subunits
271 CCT1, CCT2, and CCT3 was also increased in VLS inclusions formed by NSP5, VP2 and
272 V5-VP1 **(Fig S5b)**. Collectively, these results suggest that VP1 associates with and recruits
273 TRiC in viroplasms.

274 **VP2 requires TRiC for folding.** We reasoned that even if VP1 improved the TRiC
275 recruitment in viroplasms, it does not necessarily mean that VP1 is TRiC folding-dependent.
276 To elucidate which viroplasm RV proteins are folded by TRiC, we designed an assay using
277 TRICi and a proteasome inhibitor added to RV-infected cell cultures at different times post-

278 infection. In this assay **(Fig 8a)**, we compared the level of expression of different virus
279 proteins at 6 hpi in total extracts of RV-infected cells untreated or following treatment with
280 TRICi (at 1 hpi), assuming that those RV proteins that are TRiC-folding dependent would
281 undergo proteasome degradation and will therefore be underrepresented upon TRiC
282 inhibition. Consequently, adding the proteasome inhibitor at 3.5 hpi should rescue their
283 expression levels. Densitometry of the band intensities was performed and compared to
284 untreated cellular extracts (lane 1) of at least three independent experiments **(Fig 8b)**. As
285 depicted in **Fig 8a and b**, the only RV protein dependent on TRiC for folding corresponds to
286 VP2, which showed reduced expression in the presence of TRICi and was partially rescued
287 by treatment with UBEI-41 (70), a ubiquitin-activating enzyme E1 inhibitor. To confirm this
288 result **(Fig 8c)**, we expressed each RV protein alone and treated with TRICi and UBEI-41 at
289 3.5- and 7-hours post-transfection (hpt), respectively. The cell lysates were prepared at 22
290 hpt, and RV proteins were detected by immunoblotting using specific antibodies. Consistent
291 with our previous result **(Fig 8d)**, the densitometric analysis revealed the dependence of VP2
292 on TRiC for folding. Meanwhile, the other RV proteins tested were not sensitive to
293 TRiC/UBEI-41 treatment. In addition, in the presence of YOD1(C160S) **(Fig 8e, lanes 3 and**
294 **4)**, a dominant negative mutant for deubiquitinase YOD1 (71), and TRICi, VP2 levels were
295 even higher than in untreated samples **(Fig 8e, lane 4)**. In constrast, the expression of VP2
296 alone with TRICi resulted in a less intense band than in untreated samples **(Fig 8e, lane 2)**.
297 Collectively, the results suggest that VP2 is the primary target for TRiC-assisted folding in
298 the viroplasms.

## 299 Discussion

300 The role of TRiC in folding the mammalian orthoreovirus (MRV) σ3, another
301 member of the Reoviridae family, has been recently demonstrated to be essential for the virus

302 capsid assembly (55, 72). Using tandem mass spectrometry, we identified all TRiC subunits
303 in viroplasms of RV and found that TRiC plays an essential role in the RV life cycle,
304 specifically in the synthesis of the dsRNA genome segments. Moreover, we provide neat
305 evidence that the inhibition of TRiC results in a reduced number of viroplasms, lack of TLPs
306 in the ER, and defective DLPs lacking both encapsidated genome segments and VP1. Our
307 result demonstrated that the inhibition of TRiC impairs (-)ssRNA RV synthesis but not
308 (+)ssRNA. We also show that VP1 and VP2 are associated with TRiC. The RdRp of RV,
309 VP1, has a double task corresponding to transcription and replication. When transcribing,
310 VP1 uses as a template (-)ssRNA for synthesizing (+)ssRNA, which is required for the
311 translation of RV proteins but also as a template for replication of its genome segments. It is
312 thought that transcription occurs in two waves (73, 74). The first transcription wave takes
313 place immediately after internalization when transcriptionally active DLPs are released in the
314 cytosol, permitting the translation of RV proteins required for halting host innate immunity,
315 shutting off host translation, and building the viroplasms. The second wave of transcription
316 occurs in the viroplasms, where the generated transcripts are released to the cytosol for
317 translation by ribosomes (73, 75). The replication corresponding to the synthesis of dsRNA
318 genome segments required for virus progeny occurs only in the viroplasms. Although it has
319 been demonstrated by *in vitro* experiments the strict requirement of VP2 as a cofactor for
320 VP1 to initiate the dsRNA synthesis (6), no evidence has been provided in RV-infected cells.
321 Moreover, high-resolution cryo-electron microscopy of purified RV particles deduced that
322 the C-terminal plug of VP1 coordinates the replication process with VP2 (40, 41). The
323 replication and packaging of each of the eleven genome segments in the new core-shell is a
324 fine-tuned, not yet elucidated mechanism occurring in viroplasms. The current model (73)
325 proposes a complex of VP1 and VP3 that associates in the viroplasm, in which VP1 interacts
326 with the 3' consensus sequence of each of the eleven (+) ssRNAs. In parallel, VP2 self-

327 assembles forming decamers allowing the concomitant formation of core shells and the
328 recruitment of the VP1-VP3 complex. This process enables VP1 to replicate. In this context,
329 our results provide new evidence on RV genome replication and the packaging mechanism.
330 Consistent with the model mentioned above, we demonstrate that VP1 improves the
331 recruitment of TRiC in the viroplasms. Additionally, we demonstrate that TRiC can be found
332 surrounding structures similar to DLPs. We provide evidence that TRiC mediates VP2
333 folding. Since VP2 directly associates with VP1 (76), and because the inhibition of TRiC
334 impairs (-)ssRNA synthesis, we propose a model in which TRiC coordinates the folding of
335 high-order structures of VP2 associated with VP1 to initiate the genome replication process.
336 In this model, TRiC would then release properly folded VP2 as either a stable homo-oligomer
337 or associated with VP1 to assemble DLPs. The recruitment of TRiC in the viroplasms could
338 result in a beneficial thermodynamic environment for VP2 to promote the initiation of the
339 replication by VP1. The biochemical features of a substrate to be recognized by TRiC are not
340 well understood. Similar to MRV σ3, VP2 shares some biochemical features that could
341 render as a suitable substrate. For example, the presence of conserved and complex beta-
342 sheets in VP2 central and apical domains (77) suits with already described conditions for
343 other beta-sheet-rich substrates like tubulin or actin (46). Alternatively, TRiC can stabilize
344 VP2 higher-order structures favoring primed forms, allowing later association with VP1 and
345 formation of the core shell. Thus, TRiC can retain a polypeptide in an almost native state
346 until it binds to a protein interactor or a co-chaperone, such as Hsp70, to assist in the folding
347 of higher-order structures (78, 79).

348 The contribution of NSP5 also needs to be considered. Even if NSP5 folding shows to
349 be independent of TRiC, we found NSP5 associated with TRiC and localized in viroplasms
350 surrounding DLP-like structures. As NSP5 has been previously demonstrated to be associated
351 directly with VP1 (59) and bind RNA (80), we cannot discard the possibility that NSP5 is

352 involved in coordinating RV replication by mediation with TRiC. Similarly, other RV
353 proteins may depend on TRiC for folding. In fact, NSP3, which is not directly associated
354 with viroplasms, was redistributed in the cytosol forming small aggregates upon TRiC
355 inhibition, an indicator for misfolded proteins.

356 This study provides for the first time *in vivo* evidence explaining, at least partially, the
357 mechanism by which dsRNA genome segment replication is regulated and coordinated in the
358 RV viroplasms.

## 359 Materials And Methods

360 **Cells and viruses.** MA104 cells (embryonic rhesus monkey kidney, ATCC®CRL-2378,
361 RRID: CVCL_3845) were cultured in Dulbecco's modified Eagle's media (DMEM,
362 Gibco®BRL) supplemented with 10% fetal calf serum (FCS)(AMIMED, BioConcept,
363 Switzerland) and penicillin (100 U/ml)-streptomycin (100 µg/ml)(Gibco, Life Technologies).
364 MA-NSP5-BioID2 cell line was generated using a lentiviral system. Briefly, HEK293T cells
365 were maintained in DMEM (Life Technologies) supplemented with 10% FBS
366 (Life Technologies) and 50 µg/ml gentamycin (Biochrom AG). Approximately
367 $7\times10^6$ HEK293T cells (human embryonic kidney, RRID: CVCL_0063) were seeded in a 10
368 $cm^2$ tissue culture dish 24 hours before transfection. For each well, 2.4 µg of pMD2- VSV-G,
369 4 µg of pMDLg pRRE, 1.8 µg of pRSV-Rev, and 1.5 µg pAIP-NSP5-BioID2 were co-
370 transfected with Lipofectamine 3000 (Sigma-Aldrich) according to the manufacturer's
371 instructions. After 48 h, the virus was collected and filtered with a 0.45-µm polyvinylidene
372 fluoride filter. The virus stock was immediately used or stored at −80 °C. For lentiviral
373 transduction, MA104 cells were transduced in six-well plates with 1 ml of lentiviral
374 supernatant for 2 days. The positive cells were selected in 2 µg/ml puromycin.
375 Rotavirus porcine OSU strain (G5; P[9]), simian SA11 strain (G3; P6[1]), and rhesus RRV
376 strain (G3; P5B[3]) were propagated in MA104 cells, as described previously (81). Virus titer

377 was determined as described previously by Eichwald et al. (21) and expressed as viroplasm-
378 forming units (VFU) per milliliter.
379 **Antibodies and reagents.** Guinea pig anti-NSP5, guinea pig anti-NSP2, mouse anti-NSP2,
380 guinea pig anti-VP2, and Mouse scFV anti-NSP5 clone 1F2 were described previously (15,
381 16, 59, 82). Mouse monoclonal (mAb) anti-VP6 (clone 2F) was a gift from Dr. N. Mattion
382 (CEVAN, Buenos Aires, Argentina). Mouse mAb anti-VP7 (clone 159), mouse anti-VP5
383 (clone 4G2), and mouse mAb anti-VP2 clone (3E8) were kindly provided by Harry B.
384 Greenberg (Stanford University, CA, USA). Rabbit anti-NSP3 and mouse anti-VP1 were
385 kindly provided by Susana López (UNAM, Mexico). Rabbit anti-NSP4 was kindly provided
386 by Daniel Luque (ISCIII, Madrid, Spain). Rabbit anti-CCT1 was purchased at Invitrogen.
387 Rabbit anti-CCT2 and rabbit polyclonal anti-CCT3 (A6547) were purchased at ABclonal.
388 Goat anti-mouse conjugated to 6nm colloidal gold particles and goat anti-rabbit conjugated to
389 12 nm colloidal gold particles were purchased from Jackson ImmunoResearch Europe Ltd.
390 Mouse anti-GAPDH (clone GAPDH-71.1, RRID: AB_1078991) was purchased from Sigma-
391 Aldrich. Mouse monoclonal anti-V5 was purchased at Abcam. Rat anti-Histone H3
392 phosphorylated Ser 328 (clone HTA28) S28P-Alexa 647 (RRID: AB_397065) was purchased
393 at Biolegend. Rabbit anti-cdc20 (RRID: AB_890558) was purchased at Bethyl Laboratories,
394 Inc. Mouse monoclonal anti-dsRed2 (RRID: AB_1562589) was purchased at Santa Cruz
395 Biotechnology, Inc.
396 Streptavidin-Dylight 488 was purchased at Invitrogen. Streptavidin-HRP was purchased at
397 Sigma Aldrich.
398 MG132, Paclitaxel (taxol), and nocodazole were purchased from Sigma-Aldrich. UBEI-41
399 was purchased from NOVA biologicals. TRICi corresponds to 2-[(4- chloro-2λ4,1,3-
400 benzothiadiazol-5-yl)oxy]acetic acid, (STK526585) was chemically synthesized at Vitas M
401 Chemical (62).

402 **DNA plasmids.** pMD2.G (Addgene plasmid #12259, RRID:Addgene_12259),
403 pMDLg/pRRE (Addgene plasmid# 12251, RRID:Addgene_12251) and pRSV-Rev
404 (Addgene plasmid#12253, RRID:Addgene_12253) were a gift from Didier Trono (83).
405 pAIP(Addgene plasmid #74171, RRID:Addgene_74171) was a gift from Jeremy Luban
406 (84).

407 pAIP-NSP5-BioID2 was prepared by ligation of NSP5-BioID2 fragment in pAIP within
408 NotI and EcoRI restriction enzymes. NSP5-BiolD2 was synthesized as a gene block by
409 Genscript.

410 pcDNA-V5-VP1, pcDNA-VP1, pcDNA-VP2, pcDNA-NSP5, pcDNA-NSP3, pcDNA-VP4,
411 pcDNA-VP7, and pcDNA-VP6 were previously described (16, 18, 59, 85).

412 pCI-VP1-mCherry-(471-721)μNS was completely synthesized at Genscript (**Table S1**). pCI-
413 VP2-mCherry-(471-721)μNS, pCI-VP6-(471-721)mCherry were obtained by PCR
414 amplification of pT7-VP6-SA11 using specific primers to insert *Xho*I and *EcoR*I, followed by
415 ligation in-frame on those in pCI-mCherry-(471-721)μNS (68). pCI-VP3-mCherry-(471-
416 721)μNS was obtained by PCR amplification of pT7-VP3 (SA11) using specific primers to
417 insert *Xho*I and *Mlu*I, followed by ligation in-frame on those in pCI-mCherry-(471-721)μNS.
418 pCI-VP4-mCherry-(471-721)μNS was obtained by PCR amplification of pT7-VP4 (SA11)
419 using specific primers to insert *Nhe*I and *Mlu*I, followed by ligation in-frame on those in pCI-
420 mCherry-(471-721)μNS. pCI-VP2-mCherry-(471-721)μNS, pCI-NSP5-mCherry-(471-
421 721)μNS, pCI-NSP2-mCherry-(471-721)μNS were obtained by PCR amplification of
422 pcDNA-VP2, pcDNA-NSP5, pcDNA-NSP2 using specific primers to insert *EcoR*I and *Mlu*I,
423 followed by ligation in-frame on those sites in pCI-mCherry-(471-721)μNS. All the
424 oligonucleotides were obtained from Microsynth AG, Switzerland, and listed in Table **S1**.

425 **Pull-down assay.** MA-NSP5-BioID2 (5 x $10^6$) were infected with RV-SA11 (MOI of 5 VFU/
426 cell). For biotin labeling, cells were immediately washed after adsorption with PBS. Next, the

427 media was replaced by DMEM supplemented with 10% FBS, 50 µg/ml gentamycin, and 200
428 µM biotin (BRAND) and incubated for 17 h at 37˚C. Subsequently, the cells were gently
429 washed once in PBS and then lysed in lysis buffer (50 mM Tris pH 8.0, 500 mM NaCl, 0,1
430 mM EDTA). The cell lysate was harvested in a 1.5 ml tube and centrifuged at 13,000 rpm for
431 1 minute at 4˚C. Next, the supernatant was collected and incubated with 40 µl of Streptavidin
432 Mag Sepharose (GE Healthcare Life Sciences) in the rotator wheel for 1 h at 4°C. The beads
433 were subsequently washed three times with 500 µl of lysis buffer supplemented with 0.5 %
434 SDS, three times with lysis buffer supplemented with 1 % NP-40, and three times with lysis
435 buffer. The beads were then recovered and used for the downstream experiments.
436 **Mass spectrometry and proteomics.** MA104/NSP5-BioID2 cells (1.5 x$10^8$) were infected
437 with SA11 (MOI, 5), treated at 6 hpi with 100 µM biotin, and lysed 24 h post-transfection in
438 TNN buffer [Tris–HCl 100 mM (pH 8), NaCl 250 mM, NP-40 0.5 % with cOmplete protease
439 inhibitor cocktail (Roche)]. The pull-down of biotinylated proteins was performed using 100
440 µl StrAv Mag Sepharose™ (GE Healthcare) for each condition and incubated in a rotation
441 wheel for 3 h at 4ºC. For mass spectrometry analysis, The washed biotin pull-downs were
442 digested directly with trypsin (200 ng) in 20 µl of 20 mM Triethyl Ammonium Bicarbonate
443 pH 8.5 for 16 hours at room temperature. The supernatant was removed, the
444 beads were washed once with 50 µl of 0.1 % formic acid, and the two fractions were pooled
445 and concentrated using STAGE tips (86). The samples were resuspended in 10 µl of 0.1%
446 Formic acid and analyzed by LC-MS/MS using a NanoEASY LC (Thermo) coupled with an
447 AMAZON ETD ion trap (Bruker Daltonics). The resulting spectra were searched against the
448 human and Rotavirus proteomes using the GPM (87). Results were filtered to remove all
449 results with an e-value > 0.05. Statistical analysis and plots were performed using R (4.1.3).
450 The figure was finalized in Adobe Illustrator 2022.

451 **Immunofluorescence.** Samples were processed for immunofluorescence as described in
452 detail by Vetter *et al.*, 2022 (29). Images were acquired at CLSM and processed with
453 imageJ2 version 2.3.0/1.53q (Creative Commons license).

454 **dsRNA genome segments extraction and electropherotype.** MA104 cells seeded at a
455 density of $5x10^5$ in a 60 mm tissue culture plate were reverse transfected with 10 nM of
456 indicated siRNA and 10 µl Lipofectamine RNAiMAX Transfection Reagent (ThermoFisher
457 Scientific) in a final volume of 5 ml as described above. At 48 hpt, cells were RV-infected
458 (MOI, 25 VFU/cell). For this purpose, cell monolayers were washed once with phosphate-
459 buffered saline (PBS) (137 mM NaCl, 2.7 mM KCl, 8 mM $Na_2HPO_4$, and 2 mM $KH_2PO_4$ pH
460 7.4) and adsorbed with 500 µl of diluted virus for 1 h at 4˚C. Then, 3 ml of DMEM serum-
461 free was added to the cells and incubated at 37˚C. At 6 hpi, media was removed, and cells
462 were harvested in 500 µl of RNA extraction buffer (0.5 % NP-40, 150 mM NaCl, 1.5 mM
463 $MgCl_2$, 10 mM Tris pH 7.4) in a 1.5 ml tube. Then, the dsRNA genome was recovered by
464 extraction with 500 µl phenol-chloroform pH 4.6, followed by ethanol-sodium acetate
465 precipitation (88). The pellet was resuspended in 20 µl of distilled water and mixed with 18
466 µl Gel Loading Dye (New England Biolabs, Inc.). Samples were resolved in a 10% SDS-
467 PAGE, stained for dsRNA genome segments with visualization with GelRed (Biotium) in
468 Odyssey Fc Imager (LI-COR Biosciences).

469 **Immune and transmission electron microscopy.** For immune electron microscopy, three
470 confluent T-75 flasks of MA104 cells per sample were OSU-infected (MOI, 50 VFU/cell).
471 For this purpose, the virus was adsorbed for 1h at 4˚C and incubated in DMEM serum-free
472 for 5.5 hpi at 37˚C. Then, cells were incubated for 30 min with media containing 10 µM
473 Taxol. At 6 hpi, cells were released with trypsin, harvested in complete medium, and spinned
474 down at 1500 rpm for 2 min at room temperature. The cellular pellets were prepared
475 according to the Tokuyasu method (89). Briefly, the cells were fixed with 4% formaldehyde

476 at room temperature, washed several times with 0.1 M Na-phosphate, pH 7.4, and pelleted for
477 3 min at 13'000 rpm and 37°C in 12 % gelatin. The gelatin-embedded blocks immersed in 2.3
478 M sucrose were kept overnight at 4°C, mounted on ultramicrotome specimen holders (UC6,
479 Leica Microsystems, Wetzlar, Germany), and frozen by plunging into liquid nitrogen. After
480 trimming to a suitable block size and shape, 70 nm sections were cut at -120°C using a dry
481 diamond knife (Diatome, Biel, Switzerland). Flat ribbons were picked up with a wire loop
482 filled with a drop composed of 1 % methylcellulose, 1.15 M sucrose in 0.1 M Na-phosphate,
483 pH 7.4, and transferred onto carbon-coated formvar films mounted on 100 hexagonal
484 mesh/inch copper grids. For antigen retrieval, the sections were incubated for 1 h at 40°C
485 with 0.1 Na-phosphate buffer pH 5.5, washed with 50 mM glycine, blocked with 1% BSA,
486 and incubated with mouse monoclonal anti-NSP5 (clone 1F2) at a dilution of 1:1 and rabbit
487 anti-CCT3 (Abclonal) at a dilution of 1:5 at room temperatures for 90 minutes, washed
488 several times with 0.1% BSA. Then, the samples were incubated for 45 min at room
489 temperature with a goat anti-mouse antibody conjugated to 6 nm colloidal gold particles and
490 a goat anti-rabbit antibody conjugated with 12 nm colloidal gold particles (Jackson
491 ImmunoResearch Laboratories, Inc. West Grove, PA, USA). After incubation, the samples
492 were washed with 0.1 M Na-phosphate pH 7.4 and distilled water and transferred to a
493 mixture of 1.8 % methylcellulose and 0.4 % uranyl acetate. After 5 min incubation, the grids
494 were looped out, and the solution excess was drained and air dried to obtain a remaining thin
495 film on the grid.
496 For transmission electron microscopy images, MA104 cells were siRNA reverse transfected
497 as described above at a density of $2x10^4$ cells per well in a 24-well tissue culture plate and
498 then immediately added the sapphire discs. At 48 hpt, cells were RV-infected at MOI of 75
499 VFU/cell, fixed at 6 hpi with 2.5 % glutaraldehyde in 100 mM Na/K phosphate buffer, pH
500 7.4 for 1 h at 4˚C and kept in 100 mM Na/K phosphate buffer overnight at 4˚C. Afterward,

501 samples were post-fixed in 1% osmium tetroxide in 100 mM Na/K phosphate buffer for 1 h
502 at 4˚C and dehydrated in a graded ethanol series starting at 70 %, followed by two changes in
503 acetone, and embedded in Epon. Ultrathin sections (60 to 80 nm) were cut and stained with
504 uranyl acetate and lead citrate.
505 All the samples were analyzed in a transmission electron microscope (CM12; Philips,
506 Eindhoven, The Netherlands) equipped with a charge-coupled-device (CCD) camera (Orius
507 SC1000A 1; Gatan, Pleasanton, CA, USA) run with a Digital Micrograph software (Gatan) at
508 an acceleration of 100 kV. Images were processed for publication using Image J (version
509 2.0.0-rc-69/2.52p)
510 **Quantification of viroplasms.** Viroplasms size, number, and frequency were quantified
511 previously(21, 28). The data were processed using Microsoft ®Excel for mac (version
512 16.61.1). Statistical analysis, unpaired parametric Welch's t-test comparison post-test, and
513 plots were performed using Prism 9 for macOS version 9.3.1 (GraphPad Software, LLC).
514 **Immunoblotting.** Cells seeded in twelve multi-well tissue culture plates at a density of $2x10^5$
515 cells per well were lysed directly by adding 25 µl of Laemmli sample buffer 4X (8 % SDS,
516 40 % glycerol, 200 mM Tris-HCl pH 6.8, 0.4 % bromophenol blue). The cell extracts were
517 heated for 5 min at 95ºC, sonicated for 5 sec at 14 Hz, and loaded in SDS-polyacrylamide
518 gel. The proteins were migrated at 30 mA per gel and successively transferred to 0.45 µm
519 Protan nitrocellulose membrane (Amersham). The membranes were blocked for 30 min in
520 5% milk-PBS and then incubated with primary and the corresponding secondary antibody
521 conjugated to IRdye 680 or ICW780 (LI-COR). Samples were acquired at Odyssey Fc
522 Imager (LI-COR Biosciences).
523 **Nanopore sequencing and data analysis.** For extract preparation, MA104 cells were seeded
524 at a density of $4x10^5$ cells/ well in six multiwell plates. The next day, the cells were washed
525 twice with PBS and then infected with porcine strain OSU (MOI of 12.5 VFU/cell) diluted in

526 250 µl of DMEM serum-free. After 1 h of adsorption at 4ºC, 750 µl DMEM serum-free were
527 added to the well, and the cells were transferred to an incubator at 37ºC. For experiments,
528 including TRICi inhibitor, media was replaced at 1 hpi by adding 1.5 ml serum-free media
529 containing either 2 % DMSO or 2.5 mM TRICi. At 6 hpi, the cells were lysed and RNA
530 purified using an RNeasy mini kit (QIAGEN, Switzerland). Specifically, the genomic DNA
531 was digested in-column using DNAse I as described by the manufacturer. RNA was eluted
532 with 30 µl of nuclease-free water by incubating for 1 min before spinning down. Then, the
533 column was re-eluted using the 30 µl elution. The RNA concentration and integrity were
534 determined using 1 µl in 4150 TapeStation System (Agilent). The rest of the sample was
535 immediately frozen at -80ºC. For denaturation of dsRNA, the total purified RNA was heated
536 for 5 min at 95ºC and then immediately placed on ice. Then, the RNA sample was prepared
537 as described at Direct RNA sequencing protocol from Oxford Nanopore Technologies
538 Limited, starting with an input of 1350 ng of RNA and a specific Reverse Transcription
539 Adapter (RTA). For this purpose, specific primers binding the 5'- and 3'-UTR of each RV
540 genome segment and to GAPDH were synthesized at Microsynth AG (Switzerland) and
541 described in **Table S2.** Oligo A was diluted to 2.8 µM TN buffer (10 mM Tris-HCl pH 7.5,
542 50 mM NaCl). Next, each oligo B, corresponding to RV 5'-and 3'-UTR of each genome
543 segment, was diluted in TN buffer to 0.116 µM are added to reach a final concentration of 2.8
544 µM of total oligo B. Then, oligos were mixed 1:1 and annealed in a PCR machine (95º C for
545 2 min and then -1°C per 15 sec to 25°). This oligonucleotide was used as a replacement for
546 RTA in the nanopore protocol. The samples were loaded on MinION Mk1B and started with
547 the base calling in real-time using Guppy basecalling software version (6.0.7+c7819bc)
548 (Oxford Nanopore Technologies Limited). The data analysis was performed using Minimap2
549 software (90) followed by RStudio software version (2022.02.0+443) (RStudio: Integrated
550 Development for R. RStudio, PBC, Boston, MA URL https://www.rstudio.com/).

551 The RNA sequence coverage from ONT is found in the SRA repository with the following
552 accession reference: PRJNA900220 (https://www.ncbi.nlm.nih.gov/sra/PRJNA900220). All
553 data reported in this publication will be shared by the lead contact upon request.

554

555 **Statistical analysis.** Statistical analyses were performed using Prism 9 (version 9.4.1,
556 GraphPad Software) and RStudio software (version 2022.02.0+443, PBC, Boston, MA). The
557 error bars and statistic tests are indicated for each corresponding experiment. *p* values of
558 >0.05 were considered statistically significant (*, p<0.05; **, p<0.01; ***, p<0.001).

## 559 Acknowledgments

560 This work was supported by the University of Zurich. A pre-doctoral ICGEB
561 fellowship also supported this project for GP. The funders had no role in study design, data
562 collection, interpretation, or the decision to submit the work for publication.

563 **Author contributions**. Conceptualization, J.V., G.P., O.R.B., C.F. and C.E.; Methodology,
564 J.V., G.P., K.T., M.M., O.R.B., C.F. and C.E.; Software, J.V. and K.T.; Validation, J.V., K.T.
565 and C.E.; Formal analysis, J.V., K.T., M.M. and C.E.; Investigation, J.V., G.P., M.K., M.M.,
566 M.W., E.M.S. and C.E.; Resources, J.V., G.P., O.R.B., C.F. and C.E.; Data Curation, J.V.,
567 K.T. and C.E.; Writing-Original Draft, J.V. and C.E.; Writing-Review & Editing, J.V. and
568 C.E.; Visualization; J.V. and C.E.; Supervision, O.R.B., C.F. and C.E.; Project
569 Administration, C.E.; Funding Acquisition, O.R.B. and C.F.

## 570 Declaration of Interests

571 The authors declare that they have no conflict of interest.

## 572 References

573

574 1. McNulty MS, Curran WL, McFerran JB. 1976. The morphogenesis of a cytopathic
575 bovine rotavirus in Madin-Darby bovine kidney cells. J Gen Virol 33:503-8.

576 2. Saif LJ, Theil KW, Bohl EH. 1978. Morphogenesis of porcine rotavirus in porcine
577 kidney cell cultures and intestinal epithelial cells. J Gen Virol 39:205-17.
578 3. Altenburg BC, Graham DY, Kolb Estes M. 1980. Ultrastructural study of rotavirus
579 replication in cultured cells. Journal of General Virology 46:75-85.
580 4. Settembre EC, Chen JZ, Dormitzer PR, Grigorieff N, Harrison SC. 2011. Atomic
581 model of an infectious rotavirus particle. EMBO J 30:408-16.
582 5. Li Z, Baker ML, Jiang W, Estes MK, Prasad BV. 2009. Rotavirus architecture at
583 subnanometer resolution. J Virol 83:1754-66.
584 6. Patton JT, Jones MT, Kalbach AN, He YW, Xiaobo J. 1997. Rotavirus RNA
585 polymerase requires the core shell protein to synthesize the double-stranded RNA
586 genome. J Virol 71:9618-26.
587 7. Papa G, Venditti L, Arnoldi F, Schraner EM, Potgieter C, Borodavka A, Eichwald C,
588 Burrone OR. 2020. Recombinant rotaviruses rescued by reverse genetics reveal the
589 role of NSP5 hyperphosphorylation in the assembly of viral factories. Journal of
590 Virology 94:1-23.
591 8. Bravo JPK, Bartnik K, Venditti L, Acker J, Gail EH, Colyer A, Davidovich C, Lamb
592 DC, Tuma R, Calabrese AN, Borodavka A. 2021. Structural basis of rotavirus RNA
593 chaperone displacement and RNA annealing. Proc Natl Acad Sci U S A 118.
594 9. Criglar JM, Anish R, Hu L, Crawford SE, Sankaran B, Prasad BVV, Estes MK. 2018.
595 Phosphorylation cascade regulates the formation and maturation of rotaviral
596 replication factories. Proc Natl Acad Sci U S A 115:E12015-E12023.
597 10. Suzuki H, Konno T, Numazaki Y. 1993. Electron microscopic evidence for budding
598 process-independent assembly of double-shelled rotavirus particles during passage
599 through endoplasmic reticulum membranes. J Gen Virol 74 ( Pt 9):2015-8.
600 11. Campagna M, Eichwald C, Vascotto F, Burrone OR. 2005. RNA interference of
601 rotavirus segment 11 mRNA reveals the essential role of NSP5 in the virus replicative
602 cycle. J Gen Virol 86:1481-7.
603 12. Fabbretti E, Afrikanova I, Vascotto F, Burrone OR. 1999. Two non-structural
604 rotavirus proteins, NSP2 and NSP5, form viroplasm-like structures in vivo. J Gen
605 Virol 80 ( Pt 2):333-9.
606 13. López T, Rojas M, Ayala-Bretón C, López S, Arias CF. 2005. Reduced expression of
607 the rotavirus NSP5 gene has a pleiotropic effect on virus replication. J Gen Virol
608 86:1609-17.
609 14. Eichwald C, Jacob G, Muszynski B, Allende JE, Burrone OR. 2004. Uncoupling
610 substrate and activation functions of rotavirus NSP5: phosphorylation of Ser-67 by
611 casein kinase 1 is essential for hyperphosphorylation. Proc Natl Acad Sci U S A
612 101:16304-9.
613 15. Eichwald C, Vascotto F, Fabbretti E, Burrone OR. 2002. Rotavirus NSP5: mapping
614 phosphorylation sites and kinase activation and viroplasm localization domains. J
615 Virol 76:3461-70.
616 16. Afrikanova I, Fabbretti E, Miozzo MC, Burrone OR. 1998. Rotavirus NSP5
617 phosphorylation is up-regulated by interaction with NSP2. J Gen Virol 79 ( Pt
618 11):2679-86.
619 17. Criglar JM, Hu L, Crawford SE, Hyser JM, Broughman JR, Prasad BVV, Estes MK.
620 2014. A novel form of rotavirus NSP2 and phosphorylation-dependent NSP2-NSP5
621 interactions are associated with viroplasm assembly. Journal of Virology 88:786-798.
622 18. Contin R, Arnoldi F, Campagna M, Burrone OR. 2010. Rotavirus NSP5 orchestrates
623 recruitment of viroplasmic proteins. J Gen Virol 91:1782-93.
624 19. Buttafuoco A, Michaelsen K, Tobler K, Ackermann M, Fraefel C, Eichwald C. 2020.
625 Conserved rotavirus NSP5 and VP2 domains interact and affect viroplasm. J Virol 94.

626 20. Eichwald C, Rodriguez JF, Burrone OR. 2004. Characterization of rotavirus
627 NSP2/NSP5 interactions and the dynamics of viroplasm formation. J Gen Virol
628 85:625-34.
629 21. Eichwald C, Arnoldi F, Laimbacher AS, Schraner EM, Fraefel C, Wild P, Burrone
630 OR, Ackermann M. 2012. Rotavirus viroplasm fusion and perinuclear localization are
631 dynamic processes requiring stabilized microtubules. PLoS One 7:e47947.
632 22. Carreño-Torres JJ, Gutiérrez M, Arias CF, López S, Isa P. 2010. Characterization of
633 viroplasm formation during the early stages of rotavirus infection. Virol J 7:350.
634 23. Zhou Y, Chen L, Du J, Hu X, Xie Y, Wu J, Lin X, Yin N, Sun M, Li H. 2020.
635 MicroRNA-7 Inhibits rotavirus replication by targeting viral NSP5 in vivo and in
636 vitro. Viruses 12.
637 24. Cheung W, Gill M, Esposito A, Kaminski CF, Courousse N, Chwetzoff S, Trugnan
638 G, Keshavan N, Lever A, Desselberger U. 2010. Rotaviruses associate with cellular
639 lipid droplet components to replicate in viroplasms, and compounds disrupting or
640 blocking lipid droplets inhibit viroplasm formation and viral replication. Journal of
641 virology 84:6782-6798.
642 25. Zambrano JL, Sorondo O, Alcala A, Vizzi E, Diaz Y, Ruiz MC, Michelangeli F,
643 Liprandi F, Ludert JE. 2012. Rotavirus infection of cells in culture induces activation
644 of RhoA and changes in the actin and tubulin cytoskeleton. PLoS One 7:e47612.
645 26. Chandra P, Banerjee S, Saha P, Chawla-Sarkar M, Patra U. 2022. Sneaking into the
646 viral safe-houses: Implications of host components in regulating integrity and
647 dynamics of rotaviral replication factories. Front Cell Infect Microbiol 12:977799.
648 27. Criglar JM, Estes MK, Crawford SE. 2022. Rotavirus-induced lipid droplet
649 biogenesis is critical for virus replication. Front Physiol 13:836870.
650 28. Martínez JL, Eichwald C, Schraner EM, López S, Arias CF. 2022. Lipid metabolism
651 is involved in the association of rotavirus viroplasms with endoplasmic reticulum
652 membranes. Virology 569:29-36.
653 29. Vetter J, Papa G, Seyffert M, Gunasekera K, De Lorenzo G, Wiesendanger M,
654 Reymond JL, Fraefel C, Burrone OR, Eichwald C. 2022. Rotavirus spike protein VP4
655 mediates viroplasm assembly by association to actin filaments. J Virol:e0107422.
656 30. Cabral-Romero C, Padilla-Noriega L. 2006. Association of rotavirus viroplasms with
657 microtubules through NSP2 and NSP5. Mem Inst Oswaldo Cruz 101:603-11.
658 31. Taraporewala Z, Chen D, Patton JT. 1999. Multimers formed by the rotavirus
659 nonstructural protein NSP2 bind to RNA and have nucleoside triphosphatase activity.
660 J Virol 73:9934-43.
661 32. Martin D, Duarte M, Lepault J, Poncet D. 2010. Sequestration of free tubulin
662 molecules by the viral protein NSP2 induces microtubule depolymerization during
663 rotavirus infection. J Virol 84:2522-32.
664 33. Jing Z, Shi H, Chen J, Shi D, Liu J, Guo L, Tian J, Wu Y, Dong H, Ji Z, Zhang J,
665 Zhang L, Zhang X, Feng L. 2021. Rotavirus viroplasm biogenesis involves
666 microtubule-based dynein transport mediated by an interaction between NSP2 and
667 dynein intermediate Chain. J Virol 95:e0124621.
668 34. Geiger F, Acker J, Papa G, Wang X, Arter WE, Saar KL, Erkamp NA, Qi R, Bravo
669 JPK, Strauss S, Krainer G, Burrone OR, Jungmann R, Knowles TPJ, Engelke H,
670 Borodavka A. 2021. Liquid–liquid phase separation underpins the formation of
671 replication factories in rotaviruses. The EMBO Journal 40:e107711.
672 35. Tao Y, Farsetta DL, Nibert ML, Harrison SC. 2002. RNA synthesis in a cage--
673 structural studies of reovirus polymerase lambda3. Cell 111:733-45.

674 36. Ding K, Nguyen L, Zhou ZH. 2018. Structures of the polymerase complex and RNA
675 genome show how aquareovirus transcription machineries respond to uncoating. J
676 Virol 92.
677 37. Zhang X, Ding K, Yu X, Chang W, Sun J, Zhou ZH. 2015. In situ structures of the
678 segmented genome and RNA polymerase complex inside a dsRNA virus. Nature
679 527:531-534.
680 38. He Y, Shivakoti S, Ding K, Cui Y, Roy P, Zhou ZH. 2019. In situ structures of RNA-
681 dependent RNA polymerase inside bluetongue virus before and after uncoating. Proc
682 Natl Acad Sci U S A 116:16535-16540.
683 39. Lu X, McDonald SM, Tortorici MA, Tao YJ, Vasquez-Del Carpio R, Nibert ML,
684 Patton JT, Harrison SC. 2008. Mechanism for coordinated RNA packaging and
685 genome replication by rotavirus polymerase VP1. Structure (London, England : 1993)
686 16:1678-1678.
687 40. Ding K, Celma CC, Zhang X, Chang T, Shen W, Atanasov I, Roy P, Zhou ZH. 2019.
688 In situ structures of rotavirus polymerase in action and mechanism of mRNA
689 transcription and release. Nat Commun 10:2216.
690 41. Jenni S, Salgado EN, Herrmann T, Li Z, Grant T, Grigorieff N, Trapani S, Estrozi LF,
691 Harrison SC. 2019. In situ structure of rotavirus VP1 RNA-dependent RNA
692 polymerase. J Mol Biol 431:3124-3138.
693 42. Patton JT. 1996. Rotavirus VP1 alone specifically binds to the 3' end of viral mRNA,
694 but the interaction is not sufficient to initiate minus-strand synthesis. J Virol 70:7940-
695 7.
696 43. Lopez T, Dalton K, Frydman J. 2015. The mechanism and function of group II
697 chaperonins. J Mol Biol 427:2919-30.
698 44. Grantham J. 2020. The molecular chaperone CCT/TRiC: an essential component of
699 proteostasis and a potential modulator of protein aggregation. Front Genet 11:172.
700 45. Wang DY, Kamuda K, Montoya G, Mesa P. 2020. The TRiC/CCT chaperonin and its
701 role in uncontrolled proliferation. Adv Exp Med Biol 1243:21-40.
702 46. Kelly JJ, Tranter D, Pardon E, Chi G, Kramer H, Happonen L, Knee KM, Janz JM,
703 Steyaert J, Bulawa C, Paavilainen VO, Huiskonen JT, Yue WW. 2022. Snapshots of
704 actin and tubulin folding inside the TRiC chaperonin. Nat Struct Mol Biol 29:420-
705 429.
706 47. Bugnon Valdano M, Massimi P, Broniarczyk J, Pim D, Myers M, Gardiol D, Banks
707 L. 2021. Human Papillomavirus infection requires the CCT Chaperonin Complex. J
708 Virol.
709 48. Fislová T, Thomas B, Graef KM, Fodor E. 2010. Association of the influenza virus
710 RNA polymerase subunit PB2 with the host chaperonin CCT. J Virol 84:8691-9.
711 49. Hafirassou ML, Meertens L, Umaña-Diaz C, Labeau A, Dejarnac O, Bonnet-Madin
712 L, Kümmerer BM, Delaugerre C, Roingeard P, Vidalain PO, Amara A. 2018. A
713 global interactome map of the dengue virus NS1 identifies virus restriction and
714 dependency host factors. Cell Rep 22:1364.
715 50. Wang Y, Uraki R, Hwang J, Fikrig E. 2020. TRiC/CCT complex, a binding partner of
716 NS1 protein, supports the replication of zika virus in both mammalians and
717 mosquitoes. Viruses 12.
718 51. Inoue Y, Aizaki H, Hara H, Matsuda M, Ando T, Shimoji T, Murakami K, Masaki T,
719 Shoji I, Homma S, Matsuura Y, Miyamura T, Wakita T, Suzuki T. 2011. Chaperonin
720 TRiC/CCT participates in replication of hepatitis C virus genome via interaction with
721 the viral NS5B protein. Virology 410:38-47.

722 52. Gopal S, Perez E, Xia AY, Knowlton JJ, Cerqueira F, Dermody TS, Upton JW. 2018.
723 Murine cytomegalovirus M72 promotes acute virus replication in vivo and is a
724 substrate of the TRiC/CCT complex. Virology 522:92-105.
725 53. Zhang J, Wu X, Zan J, Wu Y, Ye C, Ruan X, Zhou J. 2013. Cellular chaperonin
726 CCTγ contributes to rabies virus replication during infection. J Virol 87:7608-21.
727 54. Wang Q, Huang WR, Chih WY, Chuang KP, Chang CD, Wu Y, Huang Y, Liu HJ.
728 2019. Cdc20 and molecular chaperone CCT2 and CCT5 are required for the Muscovy
729 duck reovirus p10.8-induced cell cycle arrest and apoptosis. Vet Microbiol 235:151-
730 163.
731 55. Knowlton JJ, Fernández de Castro I, Ashbrook AW, Gestaut DR, Zamora PF, Bauer
732 JA, Forrest JC, Frydman J, Risco C, Dermody TS. 2018. The TRiC chaperonin
733 controls reovirus replication through outer-capsid folding. Nat Microbiol 3:481-493.
734 56. Lingappa JR, Martin RL, Mei Lie W, Ganem D, Welch WJ, Lingappa VR. 1994. A
735 eukaryotic cytosolic chaperonin is associated with a high molecular weight
736 intermediate in the assembly of hepatitis B virus capsid, a multimeric particle. The
737 Journal of cell biology 125:99-112.
738 57. Hong S, Choi G, Park S, Chung AS, Hunter E, Rhee SS. 2001. Type D retrovirus Gag
739 polyprotein interacts with the cytosolic chaperonin TRiC. J Virol 75:2526-34.
740 58. Kim DI, Jensen SC, Noble KA, Kc B, Roux KH, Motamedchaboki K, Roux KJ. 2016.
741 An improved smaller biotin ligase for BioID proximity labeling. Mol Biol Cell
742 27:1188-96.
743 59. Arnoldi F, Campagna M, Eichwald C, Desselberger U, Burrone OR. 2007. Interaction
744 of rotavirus polymerase VP1 with nonstructural protein NSP5 is stronger than that
745 with NSP2. J Virol 81:2128-37.
746 60. Berois M, Sapin C, Erk I, Poncet D, Cohen J. 2003. Rotavirus nonstructural protein
747 NSP5 interacts with major core protein VP2. J Virol 77:1757-63.
748 61. Jin M, Liu C, Han W, Cong Y. 2019. TRiC/CCT Chaperonin: Structure and Function.
749 Subcell Biochem 93:625-654.
750 62. Pines A, Dijk M, Makowski M, Meulenbroek EM, Vrouwe MG, van der Weegen Y,
751 Baltissen M, French PJ, van Royen ME, Luijsterburg MS, Mullenders LH, Vermeulen
752 M, Vermeulen W, Pannu NS, van Attikum H. 2018. TRiC controls transcription
753 resumption after UV damage by regulating Cockayne syndrome protein A. Nat
754 Commun 9:1040.
755 63. Camasses A, Bogdanova A, Shevchenko A, Zachariae W. 2003. The CCT chaperonin
756 promotes activation of the anaphase-promoting complex through the generation of
757 functional Cdc20. Mol Cell 12:87-100.
758 64. Long CP, McDonald SM. 2017. Rotavirus genome replication: Some assembly
759 required. PLoS Pathog 13:e1006242.
760 65. Cao MD, Ganesamoorthy D, Elliott AG, Zhang H, Cooper MA, Coin LJ. 2016.
761 Streaming algorithms for identification of pathogens and antibiotic resistance
762 potential from real-time MinION(TM) sequencing. Gigascience 5:32.
763 66. Eichwald C, Ackermann M, Fraefel C. 2020. Mammalian orthoreovirus core protein
764 μ2 reorganizes host microtubule-organizing center components. Virology 549:13-24.
765 67. Eichwald C, Kim J, Nibert ML. 2017. Dissection of mammalian orthoreovirus μ2
766 reveals a self-associative domain required for binding to microtubules but not to
767 factory matrix protein μNS. PLoS One 12:e0184356.
768 68. Nguyen CL, Eichwald C, Nibert ML, Münger K. 2007. Human papillomavirus type
769 16 E7 oncoprotein associates with the centrosomal component gamma-tubulin. J Virol
770 81:13533-43.

69. Miller CL, Arnold MM, Broering TJ, Eichwald C, Kim J, Dinoso JB, Nibert ML. 2007. Virus-derived platforms for visualizing protein associations inside cells. Mol Cell Proteomics 6:1027-38.
70. Satheshkumar PS, Anton LC, Sanz P, Moss B. 2009. Inhibition of the ubiquitin-proteasome system prevents vaccinia virus DNA replication and expression of intermediate and late genes. J Virol 83:2469-79.
71. Ernst R, Mueller B, Ploegh HL, Schlieker C. 2009. The otubain YOD1 is a deubiquitinating enzyme that associates with p97 to facilitate protein dislocation from the ER. Mol Cell 36:28-38.
72. Knowlton JJ, Gestaut D, Ma B, Taylor G, Seven AB, Leitner A, Wilson GJ, Shanker S, Yates NA, Prasad BVV, Aebersold R, Chiu W, Frydman J, Dermody TS. 2021. Structural and functional dissection of reovirus capsid folding and assembly by the prefoldin-TRiC/CCT chaperone network. Proc Natl Acad Sci U S A 118.
73. Trask SD, McDonald SM, Patton JT. 2012. Structural insights into the coupling of virion assembly and rotavirus replication. Nat Rev Microbiol 10:165-77.
74. Guglielmi KM, McDonald SM, Patton JT. 2010. Mechanism of intraparticle synthesis of the rotavirus double-stranded RNA genome. J Biol Chem 285:18123-8.
75. Papa G, Venditti L, Braga L, Schneider E, Giacca M, Petris G, Burrone OR. 2020. CRISPR-Csy4-mediated editing of rotavirus double-stranded RNA genome. Cell Rep 32:108205.
76. Zeng CQ, Estes MK, Charpilienne A, Cohen J. 1998. The N terminus of rotavirus VP2 is necessary for encapsidation of VP1 and VP3. J Virol 72:201-8.
77. McClain B, Settembre E, Temple BR, Bellamy AR, Harrison SC. 2010. X-ray crystal structure of the rotavirus inner capsid particle at 3.8 A resolution. J Mol Biol 397:587-99.
78. Feldman DE, Spiess C, Howard DE, Frydman J. 2003. Tumorigenic mutations in VHL disrupt folding *in vivo* by interfering with chaperonin binding. Mol Cell 12:1213-24.
79. Miyata Y, Shibata T, Aoshima M, Tsubata T, Nishida E. 2014. The molecular chaperone TRiC/CCT binds to the Trp-Asp 40 (WD40) repeat protein WDR68 and promotes its folding, protein kinase DYRK1A binding, and nuclear accumulation. J Biol Chem 289:33320-32.
80. Vende P, Taraporewala ZF, Patton JT. 2002. RNA-binding activity of the rotavirus phosphoprotein NSP5 includes affinity for double-stranded RNA. J Virol 76:5291-9.
81. Arnold M, Patton JT, McDonald SM. 2009. Culturing, storage, and quantification of rotaviruses. Curr Protoc Microbiol Chapter 15:Unit 15C.3.
82. Petris G, Bestagno M, Arnoldi F, Burrone OR. 2014. New tags for recombinant protein detection and O-glycosylation reporters. PLoS One 9:e96700.
83. Dull T, Zufferey R, Kelly M, Mandel RJ, Nguyen M, Trono D, Naldini L. 1998. A third-generation lentivirus vector with a conditional packaging system. J Virol 72:8463-71.
84. Pertel T, Hausmann S, Morger D, Züger S, Guerra J, Lascano J, Reinhard C, Santoni FA, Uchil PD, Chatel L, Bisiaux A, Albert ML, Strambio-De-Castillia C, Mothes W, Pizzato M, Grütter MG, Luban J. 2011. TRIM5 is an innate immune sensor for the retrovirus capsid lattice. Nature 472:361-5.
85. De Lorenzo G, Drikic M, Papa G, Eichwald C, Burrone OR, Arnoldi F. 2016. An inhibitory motif on the 5'UTR of several rotavirus genome segments affects protein expression and reverse genetics strategies. PLoS One 11:e0166719.

819 86. Rappsilber J, Ishihama Y, Mann M. 2003. Stop and go extraction tips for matrix-
820 assisted laser desorption/ionization, nanoelectrospray, and LC/MS sample
821 pretreatment in proteomics. Anal Chem 75:663-70.
822 87. Craig R, Cortens JP, Beavis RC. 2004. Open source system for analyzing, validating,
823 and storing protein identification data. J Proteome Res 3:1234-42.
824 88. Chen D, Gombold JL, Ramig RF. 1990. Intracellular RNA synthesis directed by
825 temperature-sensitive mutants of simian rotavirus SA11. Virology 178:143-51.
826 89. Tokuyasu KT. 1973. A technique for ultracryotomy of cell suspensions and tissues. J
827 Cell Biol 57:551-65.
828 90. Li H. 2018. Minimap2: pairwise alignment for nucleotide sequences. Bioinformatics
829 34:3094-3100.
830

831 ## Figure Legends

832 **Figure 1. Tandem mass spectrometry analysis of pull-down proteins recruited to NSP5-**
833 **BioID2 in viroplasms. a)** Immunofluorescence images of RV-infected MA/NSP5-BioID2
834 cells treated with biotin either at 1 hpi (left panel) or 5 hpi (right panel) and fixed at 6 or 24
835 hpi, respectively. Viroplasms were immunostained with anti-VP2 (red), and NSP5-BioID2
836 was detected with streptavidin-dylight488 (green). Nuclei were stained with DAPI (blue).
837 Non-infected (NI) control cells are indicated at the top row. The scale bar is 10 µm. **b)**
838 Western blot of non-infected and RV-infected MA/NSP5-BioID2 cell extracts pulled down
839 with streptavidin agarose beads. The cells were treated with 100 µM biotin for the indicated
840 time post-infection ($T_x$). The membranes were incubated with anti-NSP5 (left) and
841 streptavidin-HRP (right). Red brackets indicate the NSP5 hyperphosphorylation state. **c)**
842 Mass spectrometry of virus-infected and mock-infected cells. The log(I) values were
843 normalized by subtracting the log(I) value of the NSP5 protein signal. The identified proteins
844 were ranked according to the log of the normalized intensity signal from the mass
845 spectrometry analysis. Proteins identified in the mock-infected samples were colored blue (c1
846 and c2), and proteins identified in virus-infected samples were colored red (v1 and v2). The
847 sizes of the dots are inversely proportional to the log of the p-values from the mass
848 spectrometry.

849 **Figure 2. TRiC subunits localize in viroplasms surrounding virus particles. a)**
850 Immunofluorescence of RV-infected cells immunostained at 6 hpi for the detection of
851 viroplasms (anti-NSP5, green), microtubules (anti-alpha tubulin, cyan), and TRiC subunits
852 CCT1, CCT2, and CCT3 (red). Nuclei were stained with DAPI (blue). The white dashed box
853 represents the enlarged image at the right. White arrows point to the colocalization of
854 viroplasms with TRiC subunits. The scale bar is 10 µm. Immune electron microscopy of
855 viroplasm fixed at 6 hpi. **b)** The thin sections were co-immunostained with either anti-NSP5
856 conjugated to 6 nm gold **(b)** or anti-VP6 conjugated to 6 nm gold **(c)** followed by anti-CCT3
857 conjugated to 12 nm gold. The white dashed open boxes correspond to enlarged indicated
858 images. Red arrowheads and white arrows point to the localization of CCT3 and NSP5 or
859 VP6 surrounding DLPs. The scale bar is 200 nm.
860 **Figure 3. TRiC inhibition impairs viroplasm morphology and virus progeny. a)**
861 Immunofluorescence micrograph of OSU-infected MA104 cells untreated or treated with
862 1.25 mM or 2.5 mM TRICi and fixed at 6 hpi. The drug inhibitor was added at 1 or 5 hpi as
863 indicated. Cells were immunostained to detect viroplasms (anti- NSP5, green). Nuclei were
864 stained with DAPI (blue). An enlarged image of a single cell is provided in black and white.
865 The scale bar is 10 µm. Plots for quantification of numbers **(b)** and size **(c)** of viroplasms per
866 cell after TRICi treatment from 1 to 6 hpi. Data represent the mean± SD. n> 50 cells; (****),
867 p<0.0001. **d)** Plot for virus progeny of RV-infected cells treated with TRICi during the
868 indicated time post-infection. Data represent the mean± SD of three independent
869 experiments; (****), p<0.0001. **e)** Electropherotype of RV genome segments (gs) extracted
870 at 6 hpi from RV-infected cells non-treated (NT) and treated with 1.25 mM or 2.5 mM TRICi
871 for 5 h before cell lysis. **f)** Immunofluorescence micrograph of OSU-infected cells showing
872 the distribution of RV proteins after treatment with 1.25 mM TRICi since 1 hpi. At 6 hpi,
873 cells were fixed and immunostained to detect viroplasms (anti- NSP5) and the indicated RV

874 protein (using specific antibodies for each of them). Nuclei were stained with DAPI (blue).
875 Yellow arrows point to the viroplasm position in TRICi-treated cells. The scale bar is 10 µm.
876 **Figure 4. Inhibition of TRiC leads to empty DLPs. a)** High-definition electron microscopy
877 of OSU-infected MA104 cells untreated and treated with TRICi at the indicated
878 concentrations. The inhibitor was added at 1 hpi, and the samples were fixed at 6 hpi. The
879 red, open arrowheads point to the endoplasmic reticulum surrounding viroplasms. The scale
880 bar is 500 nm. **b)** Negative staining of purified virus particles isolated from OSU-infected
881 cells untreated or treated with 1.25 mM TRICi from 1 hpi. The average size of the purified
882 particles is indicated. The scale bar is 100 nm. **c)** Immunoblot of the purified OSU virus
883 particles after treatment with or without 1.25 mM TRICi added at 1 hpi. The membranes
884 were incubated with the indicated specific antibodies. **d)** Electropherotype of OSU genome
885 segments extracted from purified virus particles of cells treated with 1.25 mM TRICi from 1
886 hpi to 6 hpi. The corresponding dsRNA genome segments are indicated.
887 **Figure 5. Rotavirus negative-strand synthesis is hampered upon inhibition of TRiC. a)**
888 Oxford nanopore technology (ONT) for direct sequencing of rotavirus positive and negative
889 sense strand RNA of the eleven genome segments at 6 hpi. The plot indicates the depth of the
890 sequence coverage of the positive (blue line) and negative (red line) sense strand RNA for the
891 eleven RV genome segments. The genome segments encoding for nonstructural and
892 structural proteins are indicated. **b)** Plot indicating the distribution of positive and negative
893 sequence reads for each of the eleven genome segments. **c)** Plot indicating the cumulative
894 ratio between positive and negative RNA sequence reads for the eleven genome segments. **d)**
895 Direct RNA sequencing using ONT of RV-infected cell extracts untreated (DMSO, upper
896 panel) or treated with 2.5 mM TRICi (TRICi, lower panel) at 6 hpi. The chemical compound
897 was added at 1 hpi until cell lysis. The plot indicates the depth of the sequence coverage of
898 the positive (blue line) and negative (red line) for the eleven RV genome segments. The

899 genome segments encoding for nonstructural and structural proteins are indicated. Plot for the
900 distribution of the positive **(e)** and negative **(f)** sequence reads of RNA isolated from DMSO
901 and TRICi-treated RV-infected cells. **(g)** Plot comparing the ratio between positive and
902 negative RNA sequence reads of RV-infected cell extracts treated with DMSO or TRICi.

903 **Figure 6. VP2 and VP1 recruit TRiC in viroplasms. a)** *In vivo* protein-protein interaction
904 platform assay using as "bait" mCh-µNS fused at N-terminal with the indicated RV-proteins.
905 The "fish" interactors correspond to the TRiC subunit, CCT3. At 24 hpt, the cells were fixed
906 and immunostained for CCT3 (anti-CCT3, green). Nuclei were stained with DAPI (blue).
907 Scale bar is 10 µm. In vivo protein-protein interaction platform for VP2-mCh-µNS (middle
908 row) and VP1-mCh-µNS (lower row) with TRiC components CCT1 **(b)** and CCT2 **(c)**.
909 Negative control mCh-µNS (upper row) is shown. At 24 hpt, cells were fixed and
910 immunostained for CCT1 (anti-CCT1, green) or CCT2 (anti-CCT2, green). Nuclei were
911 stained with DAPI. Scale bar is 10 µm. Yellow arrowheads point to mCh-µNS globular
912 cytosolic platforms. Each plot corresponds to the intensity profile of the linear region of
913 interest (LROI) indicated in the corresponding left image frame.

914 **Figure 7. VP1 enhances the recruitment of TRiC components into VLSs. a)**
915 Immunofluorescence images of VLSs composed of the indicated RV proteins. At 16 hpt, the
916 cells were fixed and immunostained to detect VLS (anti-NSP5, green) and CCT3 (anti-CCT3,
917 red). The white arrowheads point to the colocalization of CCT3 in VLS. Scale bar is 10 µm.
918 **b)** Immunofluorescence images of VLS composed of NSP5 and NSP2 in the absence (left
919 panel) and presence (right panel) of V5-VP1. At 16 hpt, the cells were fixed and
920 immunostained for the detection of VLS (anti-NSP5, green), V5-VP1 (anti-V5, red), and the
921 TRiC components CCT1, CCT2, or CCT3 (anti-CCT1, -CCT2, or -CCT3, cyan). Nuclei were
922 stained with DAPI (blue). Scale bar is 10 µm.

923 **Figure 8. VP2 folding is TRIC-dependent. a)** Immunoblotting showing the expression of
924 RV protein at 6 hpi. RV-infected cells (MOI: 25 VFU/cell) were untreated or treated with 2.5
925 mM TRICi at 1 hpi followed by treatment without or with 10 μM UBEI-41 at 3 hpi. Next, the
926 membranes were incubated with specific antibodies to detect the indicated RV proteins. **b)**
927 Plot for the expression of the indicated RV proteins normalized to the corresponding
928 untreated condition (black bar). The data correspond to at least three independent
929 experiments analyzed with one-sample t-test using a theoretical value equal to 1. (*), $p<0.05$
930 and (**), $p<0.01$. **c)** Immunoblotting showing RV proteins expressed in the absence of other
931 virus proteins at 22 hpt. At 3.5 hpt, cells were untreated or treated with 2.5 mM TRICi
932 followed by the addition, when indicated, of 10 μM UBEI-41 at 7 hpt. Then, the membranes
933 were incubated with specific RV antibodies. Except for V5-VP1, which was incubated with
934 mouse mAb anti-V5. **d)** Plot for the expression of RV proteins in the absence of other virus
935 proteins normalized to the corresponding untreated condition (black bars). The data
936 correspond to at least three independent experiments analyzed with one-sample t-test using a
937 theoretical value equal to 1. (*), $p<0.05$ and (**), $p<0.01$. **e)** Immunoblotting of cellular
938 extract co-expressing VP2 without or with Flag-YOD-1 (C160S), a dominant negative
939 deubiquitinase, after 22 hpt. The cells were untreated or treated with 2.5 mM TRICi at 3 hpt.
940 Then, the membranes were incubated with the indicated specific antibodies.
941

942 # Tables

943

944 **Table 1**. List of ranked data obtained from mass spectrometry analysis of RV-infected MA-
945 NSP5-BioID2 pulled-down extracts

| Symbol | Accession | Control 1 | | Control 2 | | RV 1 | | RV 2 | | MW [kDa] |
|---|---|---|---|---|---|---|---|---|---|---|
| | | log(e) | log(I) | log(e) | log(I) | log(e) | log(I) | log(e) | log(I) | |
| ACACA | ENSP00000344789 | -193.9 | 4.4 | -219 | 8.65 | -67.2 | 4.03 | -135.2 | 8.25 | 269.8 |
| FLNA | ENSP00000353467 | -129 | 4.28 | -204.4 | 8.73 | -34.9 | 3.76 | -206.9 | 8.67 | 279.8 |
| NSP5 | gi\|210136690\| | -59.3 | 4.59 | -98.1 | 9.28 | -113.4 | 4.99 | -143.5 | 9.57 | 21.7 |
| TCP1 | ENSP00000317334 | -2.4 | 2.78 | -69.9 | 7.99 | -14.5 | 3.24 | -87 | 7.85 | 60.3 |
| AHNAK | ENSP00000367263 | -21 | 3.63 | -66.3 | 7.74 | -1.5 | 3.1 | -7.5 | 7.19 | 628.7 |
| CCT7 | ENSP00000258091 | -6 | 3.5 | -38.3 | 7.93 | -7.7 | 3.31 | -37.1 | 7.97 | 59.3 |
| CCT4 | ENSP00000377958 | -4.1 | 3.12 | -37.6 | 7.59 | -1.8 | 3.05 | -40.8 | 7.69 | 57.9 |
| SRSF1 | ENSP00000258962 | -20.2 | 3.84 | -9.6 | 7.62 | -23.8 | 3.6 | -15.1 | 8.14 | 27.7 |
| CCT8 | ENSP00000373811 | -7.3 | 3.29 | -25.7 | 7.66 | -12.1 | 3.42 | -20.3 | 7.1 | 59.4 |
| CCT5 | ENSP00000280326 | -1.1 | 3.07 | -30.3 | 7.73 | -3.5 | 3.14 | -30.4 | 7.84 | 59.6 |
| CCT3 | ENSP00000295688 | -8.6 | 3.18 | -3.7 | 8.1 | -6.9 | 3.34 | -11.3 | 8.05 | 60.5 |
| TKFC | ENSP00000378360 | -1.5 | 2.76 | -2.9 | 7.86 | -1.4 | 2.9 | -9.3 | 8.44 | 58.9 |
| MCCC1 | ENSP00000265594 | -6 | 3.48 | -13.7 | 7.04 | | | | | |
| DVL3 | ENSP00000316054 | -2.1 | 2.76 | -4 | 7.32 | | | | | |
| VP2 | gi\|210136693\| | | | | | -40.2 | 3.94 | -53.9 | 7.58 | 102.7 |
| NSP2 | gi\|210136684\| | | | | | -32.7 | 3.9 | -38.8 | 8.19 | 36.5 |
| VP1 | gi\|210136695\| | | | | | -9.9 | 3.33 | -59.2 | 7.92 | 125.1 |

946 [a] The proteins were ranked on statistical confidence of the match.
947 [b] Control and RV correspond to non-infected and RV-infected samples—Illustrated data
948 from duplicated analysis.
949 [c] Accession: the accession number for the matched protein.
950 [d] Log (e): the statistical confidence of the match, expressed as $\log_{10}$ of the e-value.
951 [e] Log (I): measure the overall intensity of the match.
952 [f] The predicted molecular weight of the identified protein is indicated.
953

954 **Table 2:** ONT average coverage depth for (+) and (-) ssRNAs isolated from cells infected
955 with porcine OSU strain.

| RNA sequence[a)] | Average coverage depth (reads/nucleotide) | |
|---|---|---|
| | positive strand | negative strand |
| gs 1 (VP1) | 3282.45 | 196.16 |
| gs 2 (VP2) | 3901.18 | 261.65 |
| gs 3 (VP3) | 1223.30 | 271.19 |
| gs 4 (VP4) | 2109.55 | 132.48 |
| gs 5 (NSP1) | 528.93 | 671.66 |
| gs 6 (VP6) | 7705.13 | 864.61 |
| gs 7 (NSP3) | 7465.08 | 607.89 |
| gs 8 (NSP2) | 7987.08 | 343.86 |
| gs 9 (VP7) | 5845.46 | 1154.66 |
| gs 10 (NSP4) | 7906.21 | 1060.12 |
| gs 11 (NSP5) | 7858.12 | 1632.10 |
| [b)] GAPDH | 4.12 | 0.00 |

956 [a)] Rotavirus porcine strain OSU.
957 [b)] Sequence covering GAPDH of *Macaca fascicularis* (MA104 cells)
958
959
960 **Table 3:** ONT average coverage depth for (+) and (-)ssRNAs isolated of OSU infected cells
961 untreated or treated with TRICi.

| RNA sequence[a)] | Average coverage depth (reads/nucleotide) | | | |
|---|---|---|---|---|
| | DMSO | | TRICi | |
| | positive strand | negative strand | positive strand | negative strand |
| gs 1 (VP1) | 1234.23 | 90.94 | 1874.40 | 26.46 |
| gs 2 (VP2) | 2055.77 | 128.91 | 2340.52 | 33.37 |
| gs 3 (VP3) | 414.28 | 117.13 | 936.93 | 31.11 |
| gs 4 (VP4) | 1021.22 | 36.40 | 1283.85 | 9.83 |
| gs 5 (NSP1) | 1167.30 | 261.97 | 275.04 | 58.00 |
| gs 6 (VP6) | 5392.04 | 251.83 | 5365.27 | 75.08 |
| gs 7 (NSP3) | 1195.27 | 183.01 | 1986.40 | 44.96 |
| gs 8 (NSP2) | 6346.81 | 116.86 | 6825.37 | 37.34 |
| gs 9 (VP7) | 7771.91 | 226.33 | 7526.26 | 77.71 |
| gs 10 (NSP4) | 5846.58 | 345.27 | 7324.93 | 108.73 |
| gs 11 (NSP5) | 7377.46 | 383.15 | 7548.64 | 131.79 |
| [b)] GAPDH | 7.47 | 0.00 | 4.33 | 0.00 |

962 [a)] MA104 infected with porcine strain OSU
963 [b)] Sequence covering GAPDH of *Macaca fascicularis* (MA104 cells)
964
965

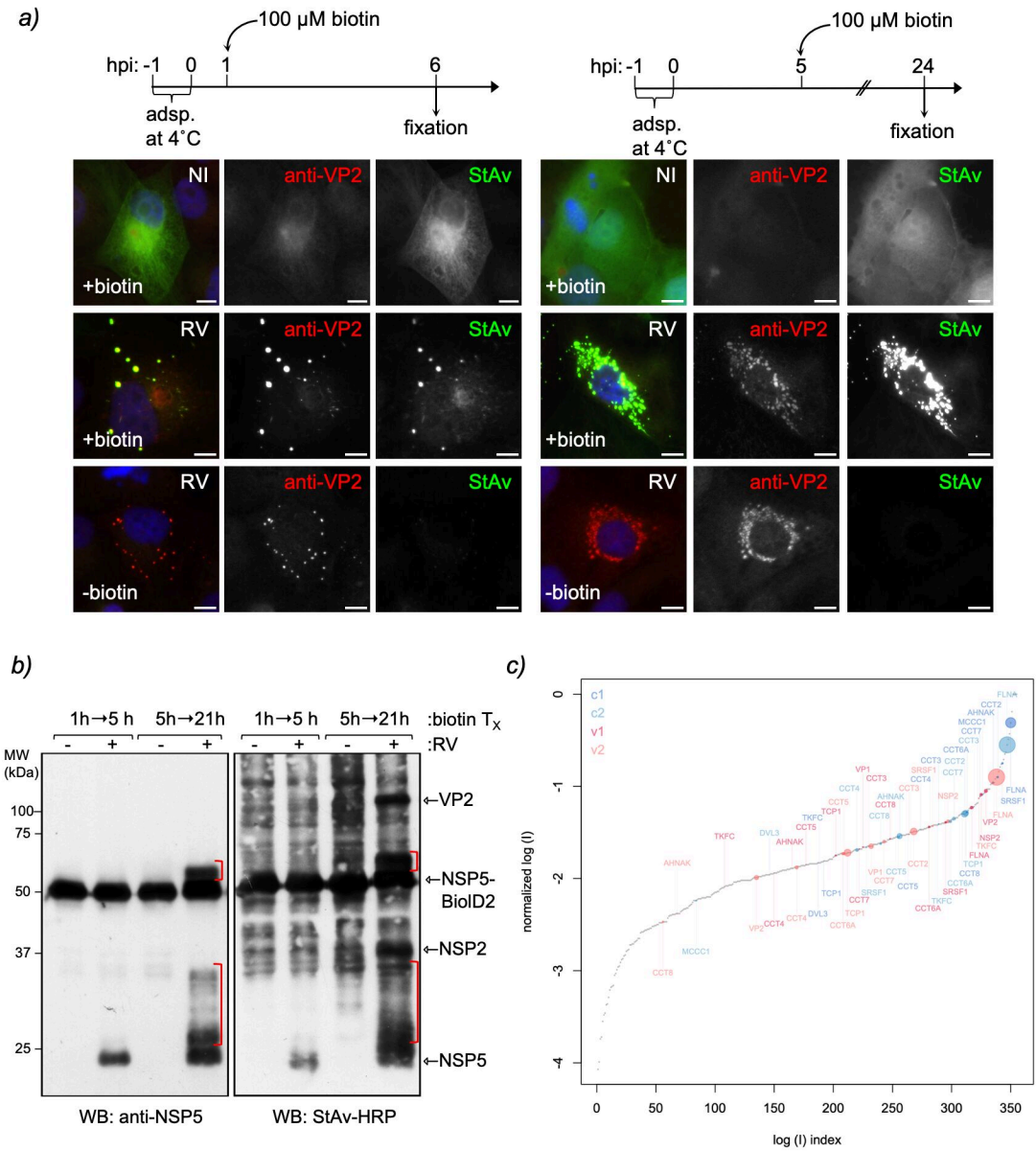
a)
100 µM biotin
hpi: -1 0 1 6
adsp. at 4˚C
fixation
100 µM biotin
hpi: -1 0 5 24
adsp. at 4˚C
fixation
NI
anti-VP2
StAv
+biotin
RV
-biotin
b)
1h→5 h
5h→21h
:biotin $T_X$
:RV
MW (kDa)
100
75
50
37
25
←VP2
←NSP5-BioID2
←NSP2
←NSP5
WB: anti-NSP5
WB: StAv-HRP
c)
c1
c2
v1
v2
normalized log (I)
log (I) index

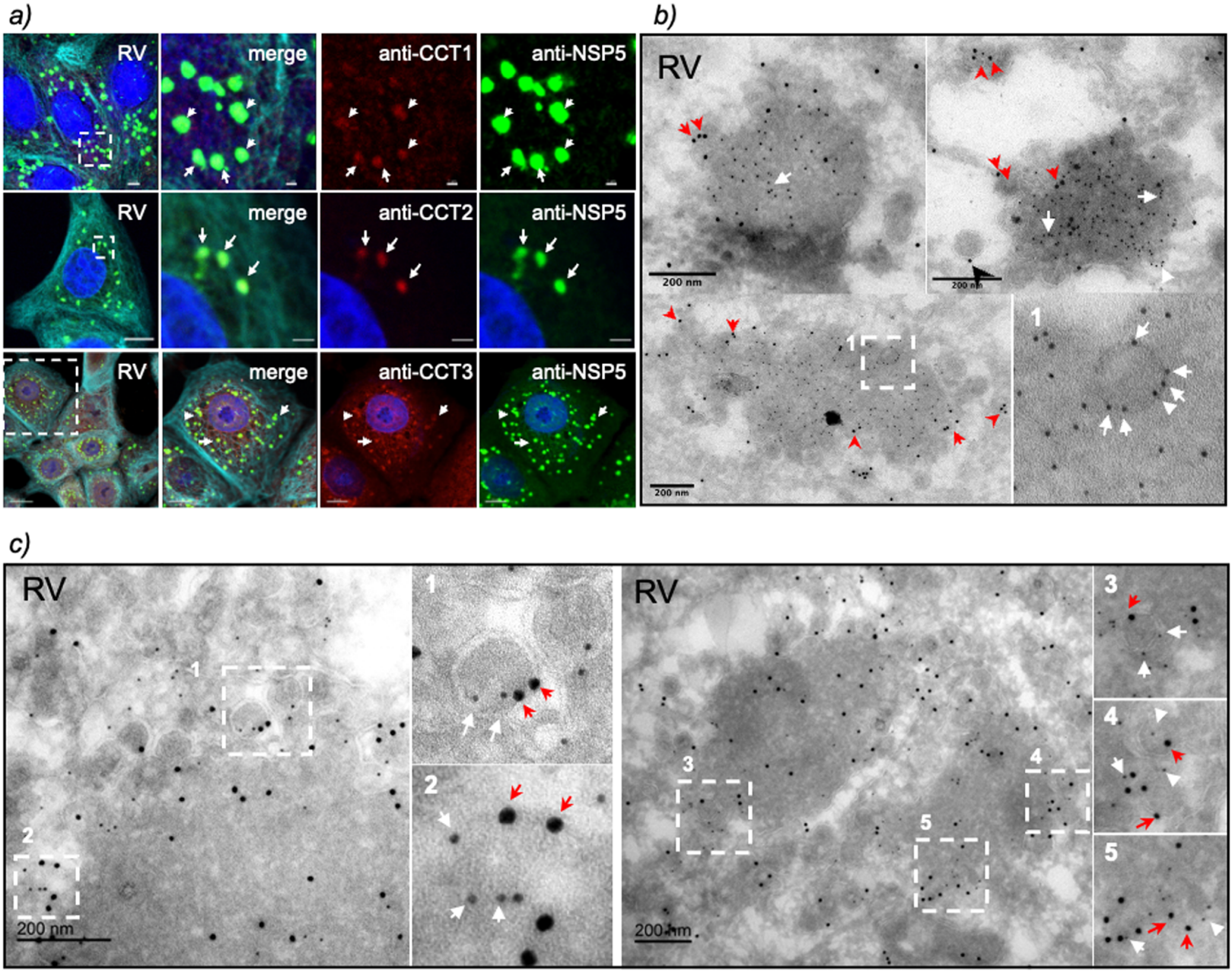
a)
RV
merge
anti-CCT1
anti-NSP5
RV
merge
anti-CCT2
anti-NSP5
RV
merge
anti-CCT3
anti-NSP5
b)
RV
200 nm
200 nm
200 nm
1
1
c)
RV
1
2
200 nm
1
2
RV
3
4
5
200 nm
3
4
5

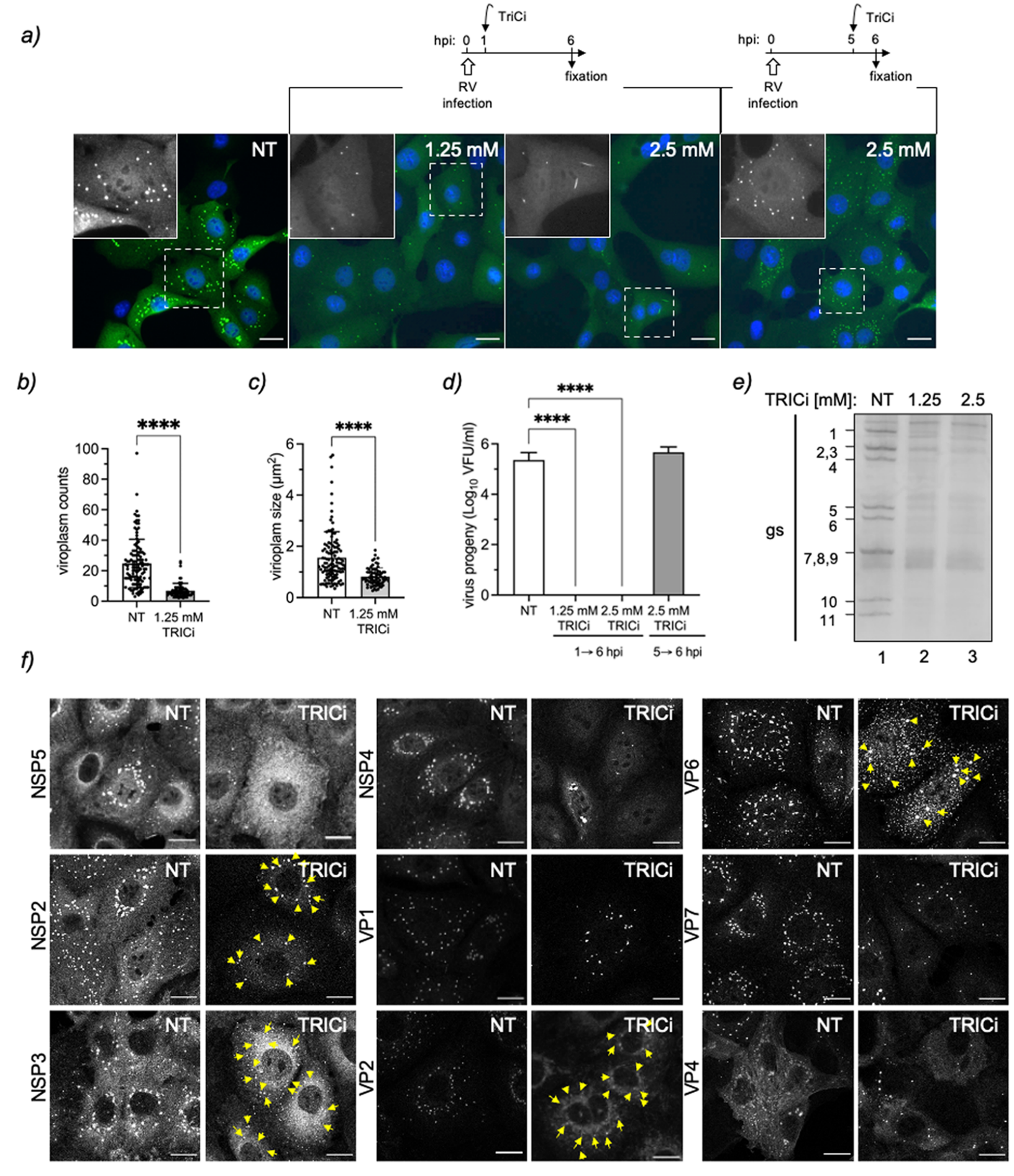
a)
TriCi
hpi: 0 1 6
RV infection
fixation
TriCi
hpi: 0 5 6
RV infection
fixation
NT
1.25 mM
2.5 mM
2.5 mM
b)
viroplasm counts
****
NT
1.25 mM TRICi
c)
virioplam size (µm²)
****
NT
1.25 mM TRICi
d)
virus progeny (Log10 VFU/ml)
****
****
NT
1.25 mM TRICi
2.5 mM TRICi
2.5 mM TRICi
1→ 6 hpi
5→ 6 hpi
e)
TRICi [mM]: NT 1.25 2.5
gs
1
2,3
4
5
6
7,8,9
10
11
1 2 3
f)
NSP5
NSP4
VP6
NSP2
VP1
VP7
NSP3
VP2
VP4
NT
TRICi

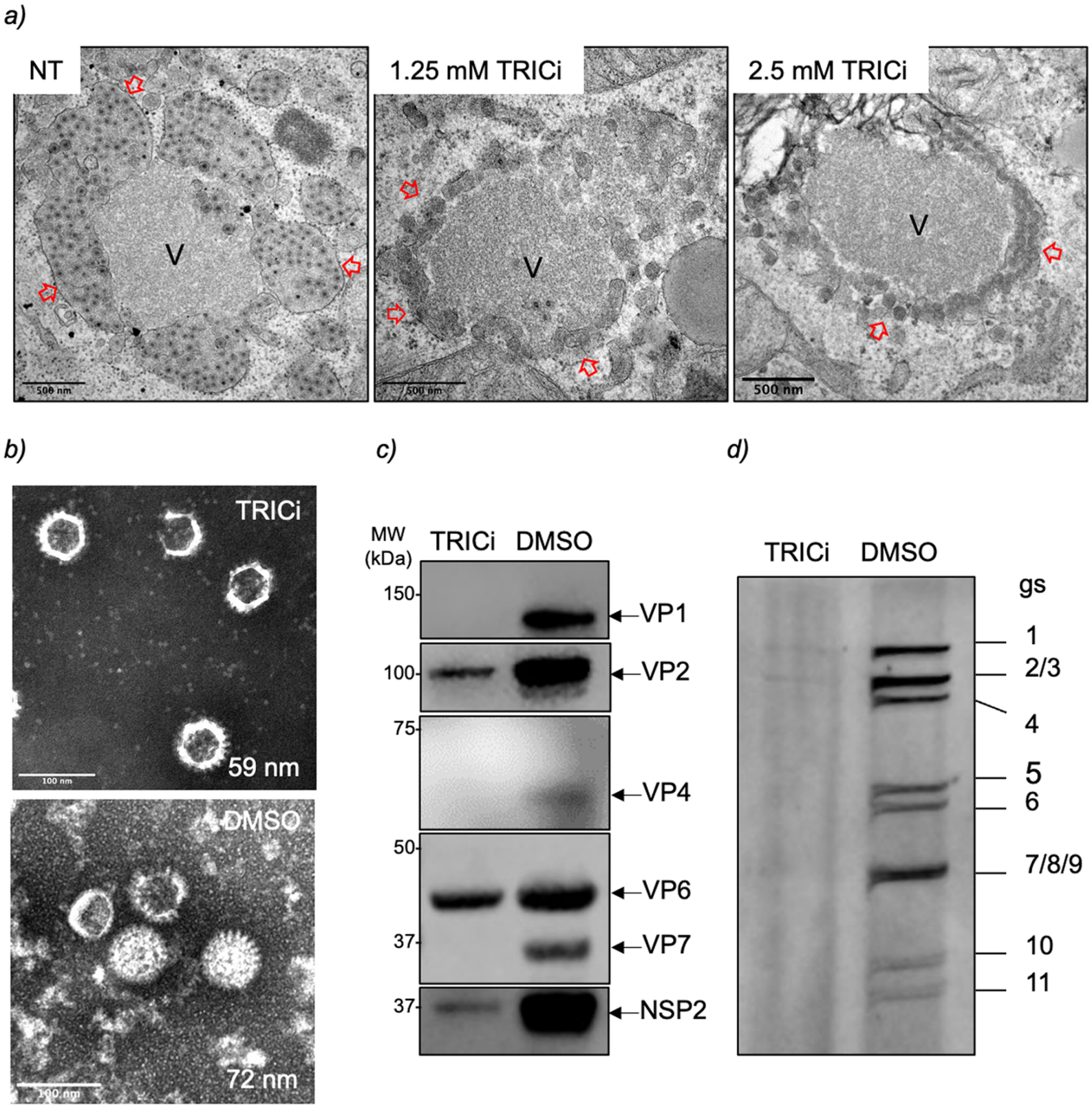
a)
NT
1.25 mM TRICi
2.5 mM TRICi
V
V
V
500 nm
500 nm
500 nm
b)
TRICi
59 nm
100 nm
DMSO
72 nm
100 nm
c)
MW
(kDa)
TRICi
DMSO
150
100
75
50
37
37
VP1
VP2
VP4
VP6
VP7
NSP2
d)
TRICi
DMSO
gs
1
2/3
4
5
6
7/8/9
10
11

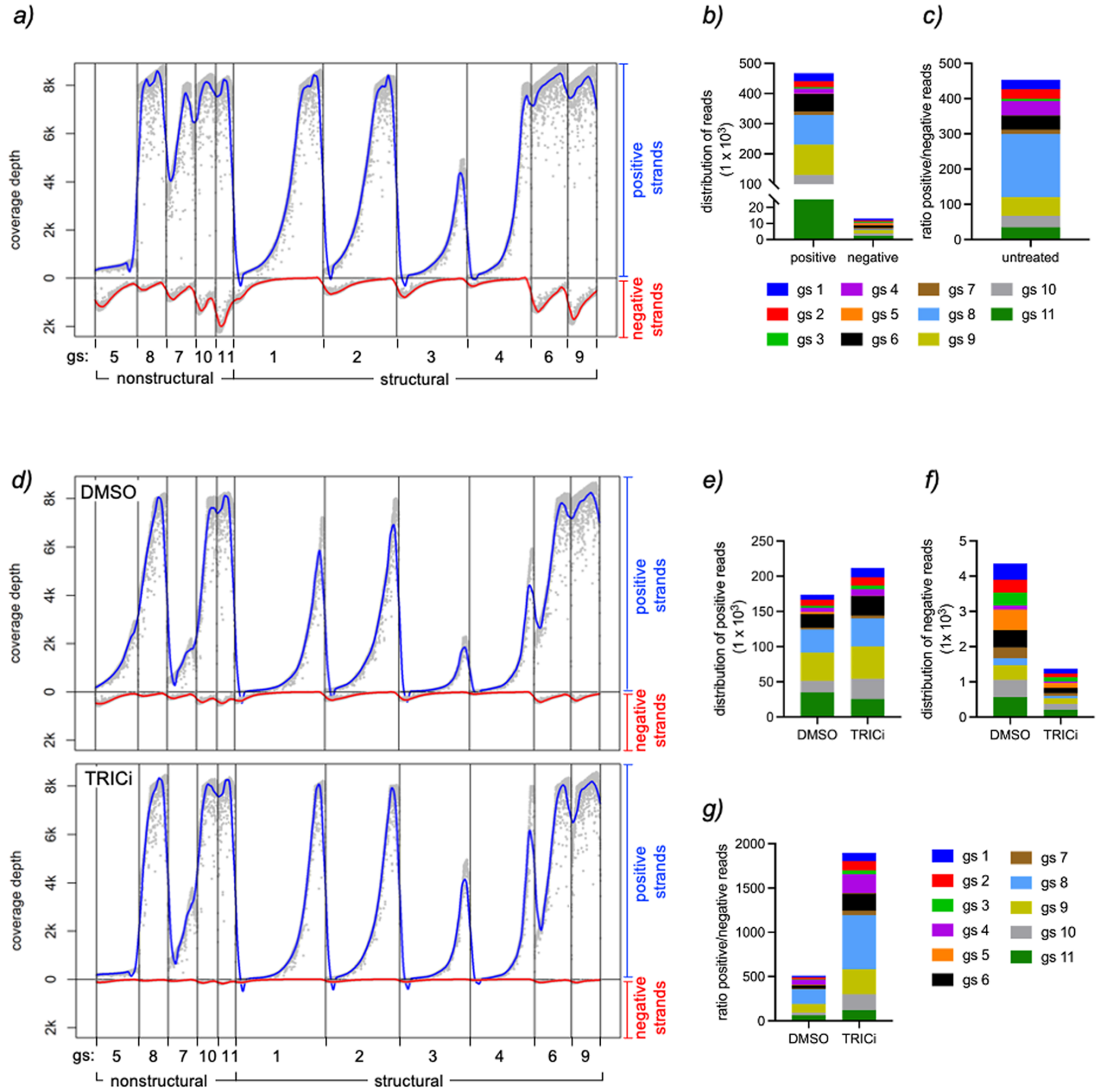
a)
coverage depth
8k
6k
4k
2k
0
2k
positive strands
negative strands
gs: 5 8 7 10 11 1 2 3 4 6 9
nonstructural
structural
b)
distribution of reads (1 x 10³)
500
400
300
200
100
20
10
0
positive
negative
c)
ratio positive/negative reads
500
400
300
200
100
0
untreated
gs 1
gs 2
gs 3
gs 4
gs 5
gs 6
gs 7
gs 8
gs 9
gs 10
gs 11
d)
DMSO
TRICi
e)
distribution of positive reads (1 x 10³)
250
200
150
100
50
0
DMSO
TRICi
f)
distribution of negative reads (1x 10³)
5
4
3
2
1
0
g)
ratio positive/negative reads
2000
1500
1000
500
0

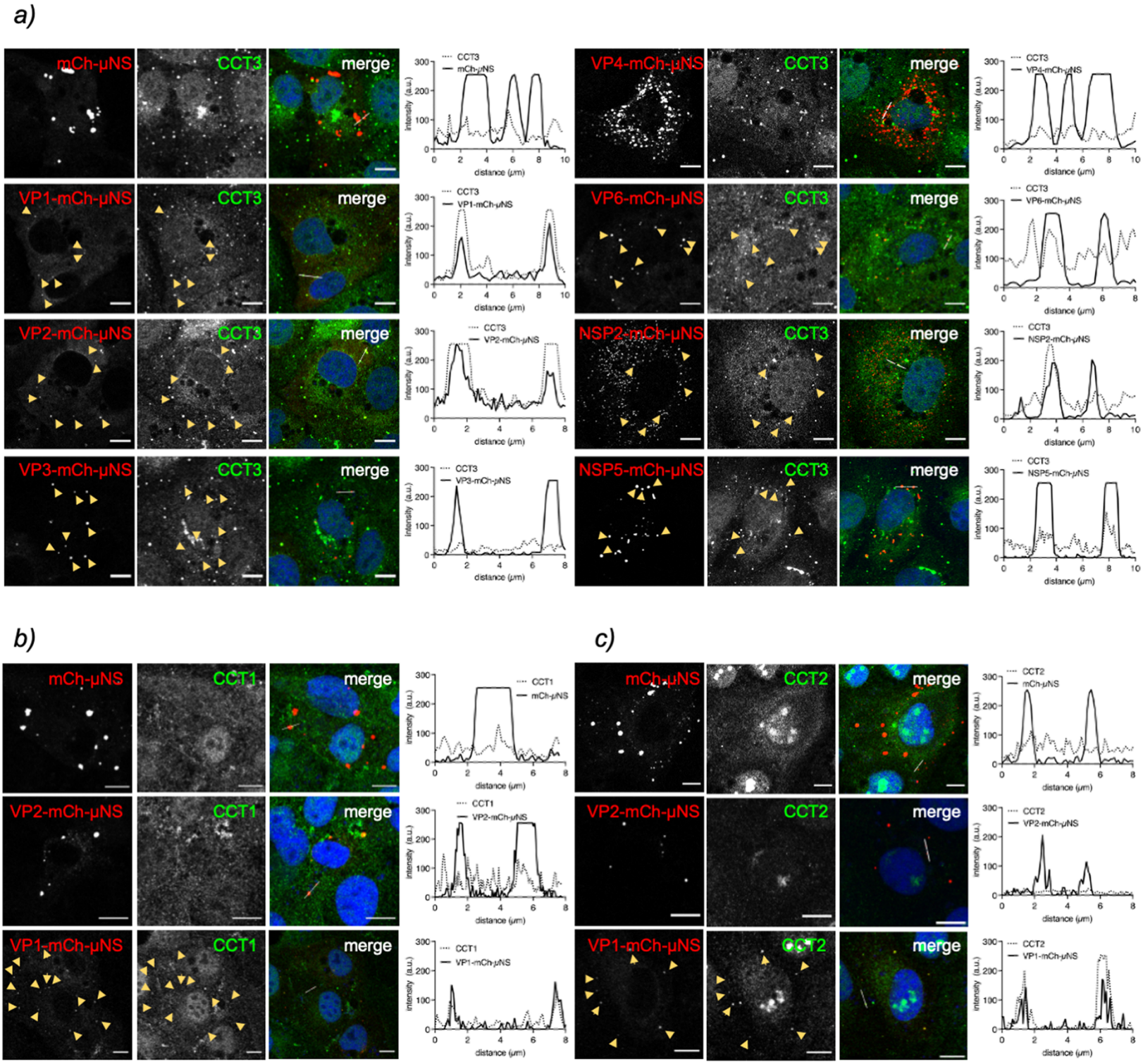
a)
mCh-μNS
CCT3
merge
VP1-mCh-μNS
VP2-mCh-μNS
VP3-mCh-μNS
VP4-mCh-μNS
VP6-mCh-μNS
NSP2-mCh-μNS
NSP5-mCh-μNS
intensity (a.u.)
distance (μm)
b)
CCT1
VP2-mCh-μNS
VP1-mCh-μNS
c)
CCT2

*a)*

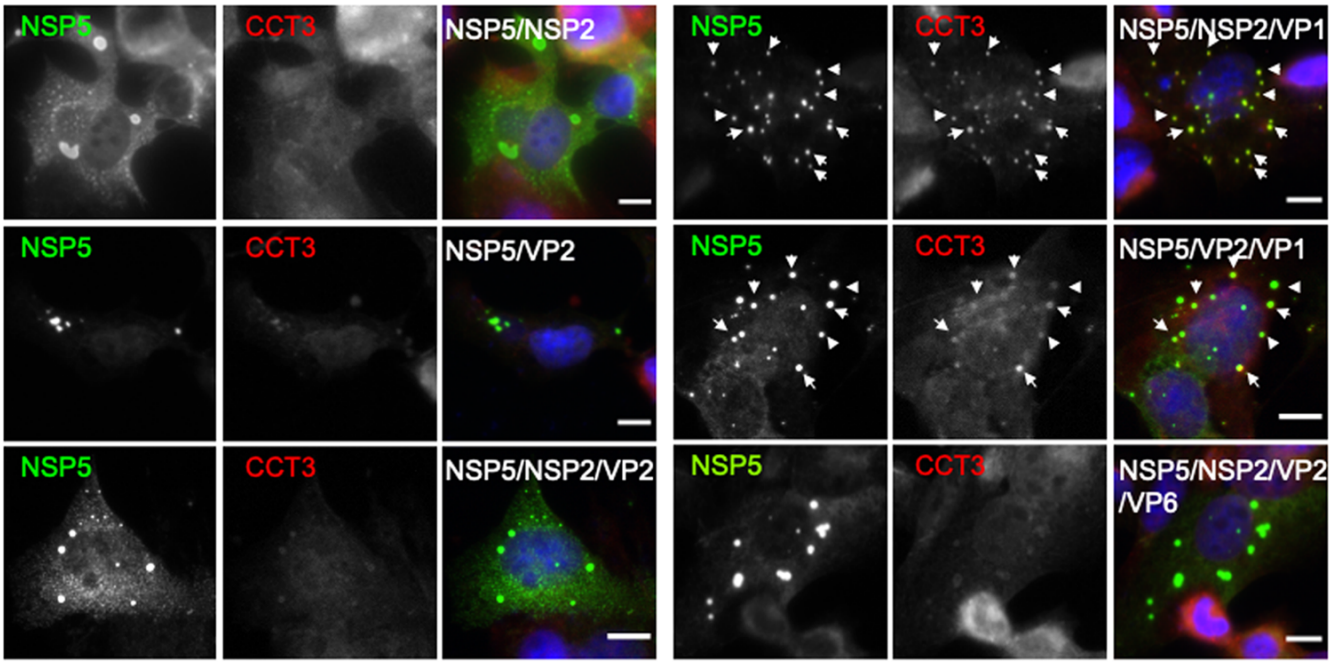
NSP5
CCT3
NSP5/NSP2
NSP5
CCT3
NSP5/NSP2/VP1
NSP5
CCT3
NSP5/VP2
NSP5
CCT3
NSP5/VP2/VP1
NSP5
CCT3
NSP5/NSP2/VP2
NSP5
CCT3
NSP5/NSP2/VP2
/VP6

*b)*

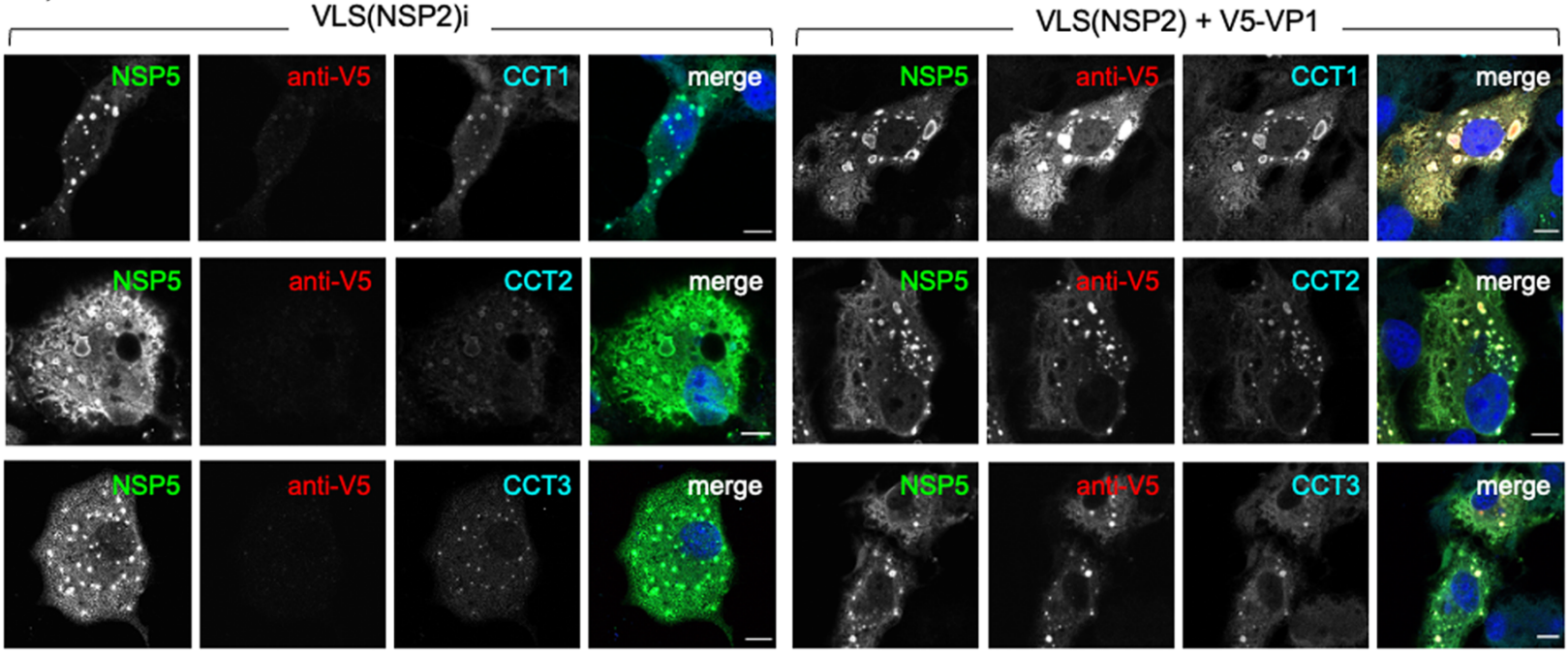
VLS(NSP2)i
VLS(NSP2) + V5-VP1
NSP5
anti-V5
CCT1
merge
NSP5
anti-V5
CCT1
merge
NSP5
anti-V5
CCT2
merge
NSP5
anti-V5
CCT2
merge
NSP5
anti-V5
CCT3
merge
NSP5
anti-V5
CCT3
merge

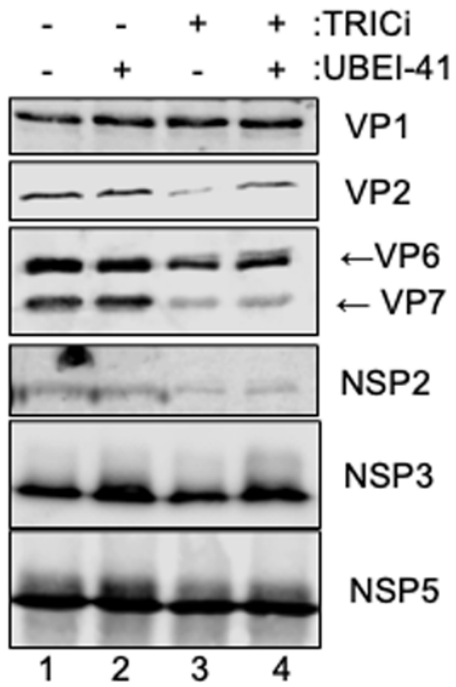
a)
- - + + :TRICi
- + - + :UBEI-41
VP1
VP2
←VP6
← VP7
NSP2
NSP3
NSP5
1 2 3 4

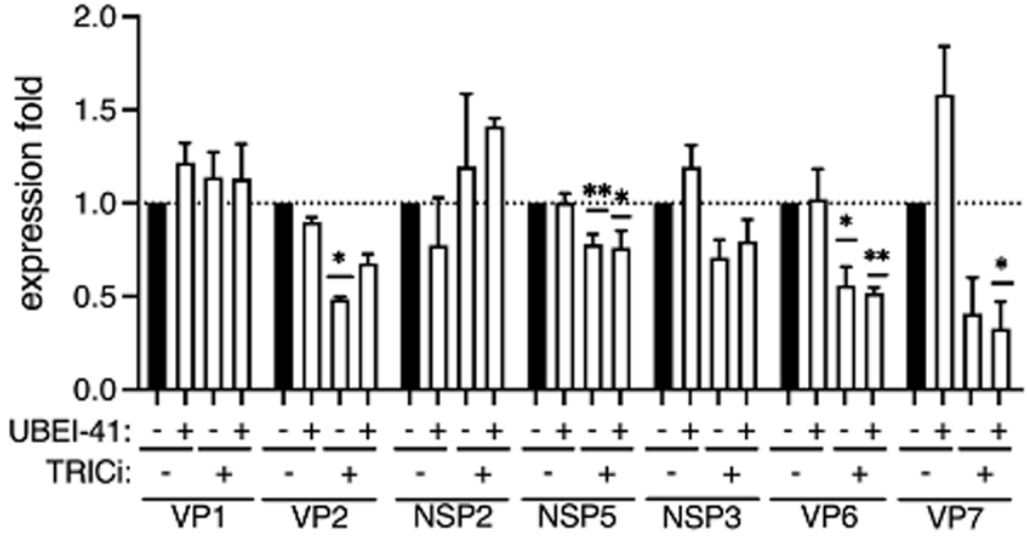
b)
expression fold
2.0
1.5
1.0
0.5
0.0
UBEI-41:
TRICi:
VP1
VP2
NSP2
NSP5
NSP3
VP6
VP7

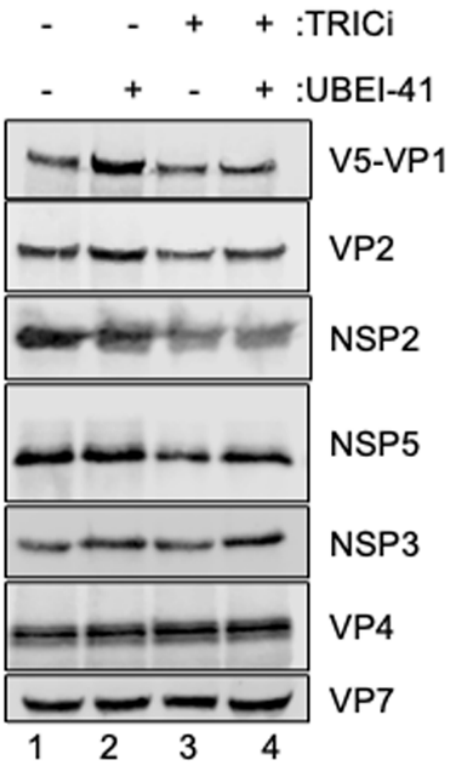
c)
- - + + :TRICi
- + - + :UBEI-41
V5-VP1
VP2
NSP2
NSP5
NSP3
VP4
VP7
1 2 3 4

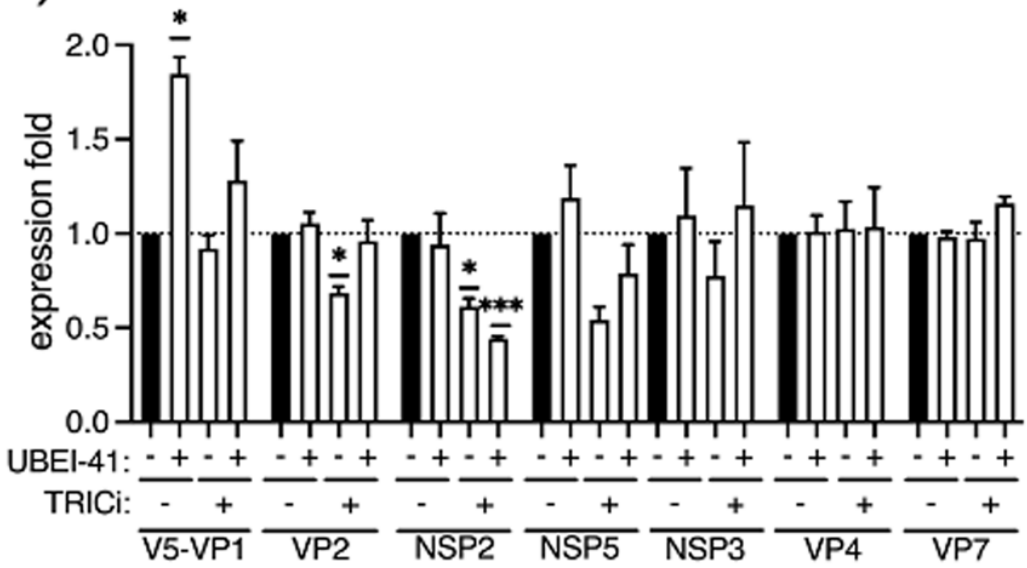
d)
expression fold
2.0
1.5
1.0
0.5
0.0
UBEI-41:
TRICi:
V5-VP1
VP2
NSP2
NSP5
NSP3
VP4
VP7

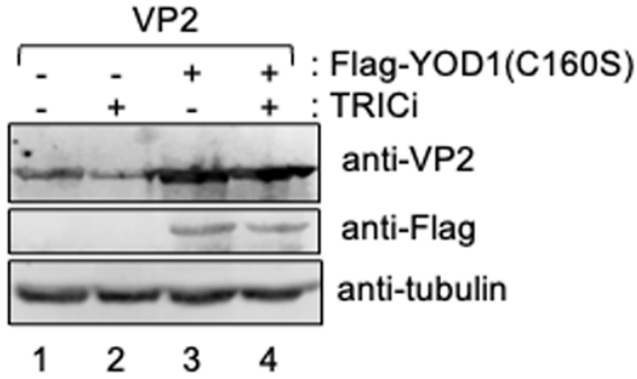
e)
VP2
- - + + : Flag-YOD1(C160S)
- + - + : TRICi
anti-VP2
anti-Flag
anti-tubulin
1 2 3 4